Intracellular amphiregulin is critical for heterochromatin maintenance and genomic stability in response to replication stress in *BRCA2*$^{mut/+}$mammary epithelial cells

Tianqi Jiang, Aiman Zein and M.A. Christine Pratt*
Department of Cellular and Molecular Medicine
University of Ottawa
Ottawa, Canada

* Author for correspondence
M.A. Christine Pratt
Department of Cellular and Molecular Medicine
University of Ottawa
451 Smyth Road
Ottawa, Ontario
Canada K1H 8M5
Email: cpratt@uottawa.ca

ABSTRACT: The BRCA2 tumor suppressor protein has roles in homologous recombination DNA repair and replication fork protection and carriers of mutation in the *BRCA2* gene (*BRCA2*$^{mut/+}$) are at high risk for breast cancers as a consequence of genomic instability. Mammary epithelial cells (MECs) are subjected to significant hormone-driven replication. *BRCA2*$^{mut/+}$ MECs must therefore be able to mitigate RS-induced chronic DNA damage that could result in cell death or senescence. In response to acute RS in hTERT-MECs, we have found that the EGFR ligand, amphiregulin (AREG) rapidly undergoes retrograde trafficking to the nucleus and nuclear membrane (NM) in association with lamin A resulting in a transient increase in H3K9me3 heterochromatin most markedly in *BRCA2*$^{mut/+}$ hTERT-MECs. RS promoted NM incorporation of prelamin A that was dependent on endogenous but not exogenous AREG. Prelamin A is reported to stabilize SUV39h1 and expression of a C-terminal truncated AREG that translocates to the NM increased SUV39h1, HP1α and H3K9me3. AREG knockdown reduced both HP1α and SUV39h1 accompanied by massive decompaction and reduction in global H3K9me3 heterochromatin. Loss of heterochromatin upon AREG depletion increased DNA damage, reduced replication fork speed and resulted in a significant increase in firing of new and multiple origins. Knockdown of endogenous AREG also impacted the NM resulting in activation of a type-1 interferon (IFN)-like response promoting senescence. Chronic RS also stimulated nuclear AREG along with *FOXM1* and *ESR1* mRNA and protein. Consistent with this, nuclear AREG, FOXM1 and ERα were detected in hyperplastic regions of human tissue. Overall, our work reveals a critical and unanticipated nuclear role for AREG in maintenance and transient induction of heterochromatin in response to RS preventing excessive DNA damage and senescence in *BRCA2*$^{mut/+}$ MECs. Since nuclear AREG also promotes ERα expression, this may link RS with aberrant expansion of estrogen receptor-expressing MECs found in *BRCA2*$^{mut/+}$ mammary tissue.

INTRODUCTION:

Amphiregulin (AREG) is a widely expressed ligand for the EGFR and has pleiotropic roles in differentiation, stem cell maintenance, proliferation, metabolism and inflammation [1]. AREG is a key factor controlling normal mammary epithelial differentiation, proliferation and ductal elongation [2]. It is synthesized as a glycosylated plasma membrane-anchored pro-protein and shedding stimuli result in cleavage of the ectodomain by ADAM17 producing a soluble N-terminal fragment containing an "EGF-like" domain which functions as an autocrine or paracrine EGFR ligand [3]. The level of ectodomain shedding is in part controlled by the endocytosis of mono-ubiquitinated full-length pro-AREG [4] which results in trafficking via the endosomal-lysosome pathway for degradation.

Decades ago, AREG was reportedly found in the nucleus of ovarian epithelial cells and cancer cells [5] and nuclear localization in fibroblasts was found to be essential for mitogenic activity [6]. Unlike EGF, AREG contains an NLS [7] and a portion of the endocytosed AREG can undergo retrograde transport to the inner NM where it interacts with lamin A, a major component of the nuclear lamina resulting in marked global increases in heterochromatin [8]. The biological stimulus governing nuclear trafficking of AREG and its association with lamin A as well as the underlying mechanism of increased H3K9 methylation are not known.

In mammalian cells, heterochromatin is established by families of H3K9-specific histone methyltransferases (HMTs). The suppressor of variegation 3-9 (SUV39)-family proteins are associated with di- and tri-methylation of H3K9 at centromeric and telomeric regions [9]. During the replication of constitutive heterochromatin, Suv39h1/2 can bind to the parental histones containing H3K9me2/3 resulting in histone methylation on the new histone [10]. The chromodomain of heterochromatin protein 1α (HP1α) binds H3K9me and can then dimerize and multimerize [11,12], bridging nucleosomes which may help stabilize the nascent heterochromatin domains [13,14] resulting in the spread of H3K9me3 over large regions [15].

Constitutive heterochromatin is enriched for di- and trimethylated histone H3 lysine 9 (H3K9me2 and H3K9me3 respectively) and represents approximately 50% of the human genome [16]. H3K9me2/3 maintains repression of gene expression in a cell lineage specific manner [17], silences repeats and transposable elements and related elements [18,19] and dictates genome replication timing during S phase [20-22] which is also integral to maintenance of the epigenetic state

of the cell [23]. Most constitutive heterochromatin is situated at pericentromeric and telomeric domains of chromosomes and localized to perinucleolar regions and the nuclear periphery where it is tethered to the nuclear lamina in regions known as lamina associated domains (LADs) [24]. Heterochromatin associates with the nuclear lamina directly through heterochromatin protein (HP1α) which binds the lamin B receptor and also via the proline-rich PRR14 protein which interacts with lamin A/C [25-26].

Lamin A forms part of the inner NM matrix and is synthesized as prelamin A which then undergoes several C-terminal post-translational modifications including farnesylation and methylation followed by cleavage of the prenylated CAAX motif by the ZMPSTE24 metalloprotease. A mutation in *LMNA* gene resulting in production of progerin [27-28] and cells lacking the ZMPSTE24 protease result in accumulation of stable forms of prelamin A which exhibit aberrant nuclear morphology and characteristics of premature aging [29]. Accumulation of prelamin A forms in ZMPSTE24 deficient cells and cells engineered to express progerin are associated with increased H3K9me3 heterochromatin as a consequence of enhanced binding of prelamin A with SUV39h1 promoting its stabilization [30].

Replication stress (RS) is recognized as a significant contributor to genomic instability that can lead to transformation [31]. RS can result from numerous impediments to replication fork progression including collisions of the replication-transcription complexes and nucleotide depletion [32].The BRCA2 protein has a key role in preventing DNA damage in response to RS by participating in homologous recombination and replication fork protection. *BRCA2*$^{mut/+}$ mammary epithelial cells (MECs**)** are differentially sensitive to RS-induced DNA damage [33-34]. The stalled fork results in exposure of unwound single-stranded DNA that is rapidly coated with replication protein A (RPA) to prevent nucleolytic attack and helps recruit RAD51 which, along with DNA translocases, facilitates fork reversal to allow fork repair or restart to reduce fork breakage [35]. BRCA2 mediates the loading of RAD51 onto ssDNA at stalled and reversed forks [36,37] protecting the reversed fork from excessive degradation by nucleases [38] and ultimately DNA breaks. Thus mechanisms that reduce excessive levels of RS-induced chronic DNA damage which may result in senescence and or apoptosis would be critical for supporting the ongoing proliferation of *BRCA2*$^{mut/+}$ MECs.

Aside from constitutive heterochromatin, H3K9me3 also forms locally and transiently at stalled replication forks both in yeast [39] and in mammalian cells [40] and maintains fork stability

associated with the compaction of chromatin, forming an environment that retains fork protection and remodeling factors until the stress is resolved [40]. Transient formation of heterochromatin is also critical in the response to DNA double-strand breaks (DSBs) in euchromatin. DSBs activate the mre11–rad50–nbs1 (MRN) complex at DNA ends which then recruits the Tip60 acetyltransferase which activates ataxia telangiectasia-mutated (ATM) kinase responsible for the phosphorylation of DSB repair proteins [41]. Tip60 recruitment depends on H3K9 methylation which is actively increased at DSBs in regions of low H3K9me3 density to allow for efficient DSB repair in euchromatin. The rapid heterochromatinization occurs over kilobases surrounding the DNA break and is removed once the break is repaired [42].

Here, we report our discovery that AREG promotes heterochromatin maintenance in MECs and, in response to DNA damage, AREG protein is processed and undergoes increased nuclear trafficking in association with lamin A. Expression of a C-terminal AREG mutant that translocates to the nucleus increases HP1α and SUV39h1 in conjunction with enhanced nuclear prelamin A and heterochromatin formation. Depletion of endogenous AREG significantly reduced global H3K9me3 levels and resulted in decompaction, altered DNA replication dynamics, increased stalled forks and the formation of DSBs. Moreover, AREG depletion had profound effects on the NM including disruption of the Ran-GTPase gradient, reducing nuclear content of DNA repair proteins. Lastly, we show that chronic RS increases nuclear AREG and results in the induction of FOXM1 and ERα expression. Overall, through maintenance of constitutive heterochromatin and promotion of the transient increase in heterochromatin that accompanies RS and DSBs, we propose that nuclear translocation of AREG helps maintain genomic stability critically important in *BRCA2*$^{mut/+}$ MECs where chronic DNA damage could lead to senescence or cell death.

RESULTS:

Replication stress promotes AREG stabilization and increases nuclear membrane localization. Although AREG is best characterized as an EGFR ligand, the presence of nuclear AREG in cancer and normal cells has been documented in several studies [5,43,44]. To investigate this further in the context of the mammary gland, we began by analyzing the endogenous expression of AREG in hTERT-immortalized MEC isolates derived from two different normal and 2 BRCA2$^{mut/+}$ hTERT-immortalized primary MECs. A report byS1

Isokane and colleagues [8] demonstrated that treatment with phorbol ester which activates the stress kinase p38, results in a portion of unshed proAREG entering the endoplasmic reticulum, undergoing retrograde nuclear trafficking via the trans-Golgi network, endoplasmic reticulum (ER) retrieval and finally nuclear localization in association with lamin A in HeLa cells. *BRCA2*$^{mut/+}$ MECs are sensitive to replication stress resulting in DNA damage which activates p38 [45]. We therefore treated cells with hydroxyurea (HU) (4mM for 4hrs) to induce replication stress. Immunofluorescence (IF) of untreated MECs shows the typical distribution of AREG primarily at the plasma membrane (Figure 1A). In contrast, HU-treated MECs showed increased nuclear AREG which was randomly colocalized at and within the inner NM with lamin A. We next performed immunoblotting to evaluate the effects of RS on AREG protein in all cell isolates. Similar to the array of AREG peptides found in breast cancer cell lines [46], both normal and *BRCA2*$^{mut/+}$ MECs expressed baseline levels of 37kDa-40kDa AREG and AREG and additional bands of 23kDa, 18kDa and 16kDa. The antibody used recognizes regions from aa107-184 indicating that all bands contained sequences within the EGF-like domain and C-terminus. Notably, RS resulted in a marked increase in the 23kDa and 18kDa species and a diminution of the 16kDa band suggesting that the latter is derived from these larger peptides. This was most profound in *BRCA2*$^{mut/+}$ MECs and increased up to 3h following washout of HU (Figure 1B). HU resulted in an approximate 2-fold increase in AREG mRNA (Figure 1C) which could contribute to an increase in total AREG protein.

Using antibody against full length AREG, we next assessed the effect of acute RS on the subcellular location of AREG in cytoplasmic and nuclear fractions in *BRCA2*$^{mut/+}$ MECs with or without RS (Figure 1D). In control conditions, the 23kDa AREG was present in the cytoplasm and to lesser extent was also found in the nuclear fraction. While the 23kDa peptide did not change following HU, the 18kDa nuclear band was increased, consistent with an overall increase in nuclear AREG. Together, these results suggest that intracellular AREG undergoes cleavage and a constitutive level of the 23kDa species is present in the nucleus in unperturbed MECs. RS increases nuclear residence of the 23kDa and 18kDa AREG peptides, in part due to diversion from lysosomal degradation.

Replication stress induces AREG:lamin A interaction and the association of AREG with early endosomes: A previous report showed that nuclear trafficked AREG interacts directly with lamin

A assessed by immunoprecipitation [8]. To determine the impact of RS on the proximity of AREG to lamin A, we performed a proximity ligation analysis (PLA) which detects colocalization of proteins at a distance of <40nm. Using AREG and lamin A antibodies, very few PLA foci were present in untreated cells, however foci were significantly increased following the 4 hr treatment with HU. Foci were found in the cytoplasm (ER) as well as at the nuclear periphery and nucleoplasm (Figures 2A, 2B). The increase in nuclear AREG in response to 4hr of HU induced RS suggests rapid nuclear trafficking.

ProAREG undergoes endocytosis following monoubiquitination of K240 and is rapidly incorporated into early EEA1-positive endosomes. In unperturbed cells, a portion of AREG traffics from early to late endosomes and ultimately to autophagic lysosomes for degradation [4]. Dual IF for AREG and the early endosome marker, EEA1, was performed in untreated and HU-treated MECs. In both normal and *BRCA2*$^{mut/+}$ MECs, some AREG was detected at nuclear membranes independent of EEA1 and may represent previously deposited AREG. However, AREG at the nuclear periphery and in the cytoplasm were largely associated with EEA1-marked endosomes. A 4h treatment with HU prompted a significant increase in peripheral NM location of EEA1/AREG and colocalization in both *BRCA2*$^{mut/+}$ and normal MECs (Figure 2C, 2D). Notably, lamin A nuclear import is regulated by sorting nexin 6 (SNX6) through a RAN-GTP-dependent mechanism and does not enter the ER [47]. AREG has a putative C-terminal ER-retrieval motif and can bind to lamin A [8], thus interaction at the surface of the ER may account for the significant increase in lamin A:AREG PLA foci seen in HU treated MECs.

p38α can also stimulate endocytosis [48] and can phosphorylate the Rab5 effector EEA1 to regulate the recruitment to membranes [49]. Since *BRCA2*$^{mut/+}$ MECs are deficient in HR and fork protection and are therefore prone to DNA damage, we performed IB for P-p38. P-p38 was strongly induced by HU in *BRCA2*$^{mut/+}$ MECs compared to normal MECs (Figure 2E) and activation was commensurate with the increased level of AREG protein. We therefore tested the effect of p38 inhibitor SB203580 on the induction of AREG following HU treatment. Figures 2F and 2G show that inhibition of p38 prevented the HU-mediated increase in AREG protein and strongly reduced nuclear periphery localization of EEA1 endosomes. Together these results are consistent with RS induction of DNA damage most strongly in *BRCA2*$^{mut/+}$ MECs which activates p38α and promotes EEA1 early endosome trafficking of AREG.

Endogenous AREG promotes H3K9me3 formation by modulating the nuclear prelamin A level and regulating HP1α and SUV39h1. Previous studies showed that enforced expression of AREG lacking the C-terminal 11 amino acids results in NM localization, interaction with lamin A and strongly enhances H3K9me3 heterochromatin [8]. Since AREG undergoes significant nuclear trafficking following HU treatment we therefore analyzed the formation of H3K9me3 after HU-induced replication stress in siAREG vs siNT-transfected MECs. Immunoblot analysis in Figure 3A revealed that, as expected, HU transiently increased H3K9me3, however, AREG KD strongly reduced both baseline and HU-induced transient H3K9me3 assessed by immunoblot. Levels of H3K9me3 returned to baseline within 10 minutes following removal of HU in siNT-transfected MECs but remained repressed in AREG-depleted MECs (*Figure S1A*). Interestingly, the level of H3K9me3 was reduced below baseline in normal MECs following washout of HU, which may be consistent with the accumulation of KDM3A demethylase at stalled forks which gains access to chromatin of upon replication restart [40].

To determine if the nuclear trafficking of AREG and formation of H3K9me3 is induced by a different RS stimulus, we tested the effect of inhibition of Ataxia Telangiectasia-rad related (ATR) kinase. This enzyme orchestrates the response to ssDNA gaps that occur upon replication stress [50,51]. ATR kinase and its target kinase, CHK1, have additional roles in protecting the genome including the suppression of origin firing in damaged cells which limits the number of replication forks, thereby preventing excessive ssDNA accumulation, exhaustion of the nuclear RPA pool, and replication fork collapse [32,52,53]. In contrast, in unchallenged cells, ATR-deficiency enhances RS and aberrantly increases perinuclear heterochromatin [54,55]. We first determined the effect of the ATR inhibitor VE-821 on basal and HU-induced AREG protein and H3K9 heterochromatin formation (*Figure S1B*). As expected, HU robustly induced H3K9me3, however the combination of VE-821 and HU completely blocked this response. Additionally, the increase in AREG protein was also prevented. ATR inhibition also reduced nuclear AREG detection by IF in MECs treated with HU (*Figure S1C*). Thus, ATR activation is critical for the RS-induced AREG protein increase as well as H3K9me3 formation. In contrast, treatment with VE-821 alone for 3hrs in *BRCA2*$^{mut/+}$ MECs strongly enhanced AREG protein detection in the ER and at the NM while increasing both AREG protein and H3K9me3 levels. Thus, ATR inhibition and associated RS produces a similar increase in H3K9me3 and AREG protein as that obtained with HU. Overall, these data demonstrate that endogenous AREG regulates H3K9me3 heterochromatin and extend these findings to reveal

that RS originating in different ways can function as a stimulus for AREG nuclear trafficking in association with lamin A.

H3K9me2/3-marked constitutive heterochromatin interacts at the nuclear periphery in lamina associated domains (LADs) [56,57]. Both heterochromatin protein-1 (HP1) and lamin A/C participate in tethering of LADs at the lamina [26,58]. To determine the effect of AREG depletion on heterochromatin domains, we next performed confocal imaging of H3K9me3 IF in *BRCA2*$^{mut/+}$ MECs transfected with AREG or NT siRNAs and treated with or without HU are shown in Figure 3B. In siNT-transfected MECs, H3K9me3 was located at the nuclear periphery and in punctate domains within the nucleoplasm. In contrast, in a majority of cells, siAREG reduced overall H3K9me3 mean fluorescence intensity (MFI) (Figure 3C) although some cells showed increased intensity of H3K9me3 IF but with a highly diffuse pattern. AREG KD strongly prevented localization at the nuclear periphery (Figures 3B, 3D). HU treatment in control MECs resulted in redistribution of H3K9me3 to the nuclear interior in a honeycomb pattern, while H3K9me3 in AREG-depleted MECs remained low and diffuse following HU treatment. 3D images (Figure 3E) generated using Imaris of H3K9me3 in MECs subjected to the same conditions as in B. Perinuclear and nucleoplasmic foci were evident in siNT-transfected MECs, while HU induced the formation of nucleoplasmic foci. In contrast, AREG-depleted MEC contained highly diffused regions of decompacted heterochromatin or loss of H3K9me3 and large numbers of small puncta formed after HU treatment.

The PLA in Figure 2A indicated that a major cytoplasmic and nuclear recruitment of AREG associated lamin A occurs in response to RS. This interaction was evident in both the nuclear interior and at the periphery. Farnesylated prelamin A enters the nucleus where it is rapidly processed via ZMPSTE24-mediated cleavage to yield mature lamin A which forms dimeric antiparallel coiled coils [59]. Progerin or defective ZMPSTE24 result in the persistence of uncleaved prelamin A which was shown to bind and stabilize SUV39h1 and resulting in increased H3K9me3 formation [30]. Thus, the presence of prelamin is anticipated to increase heterochromatin. We therefore reasoned that in response to RS or DNA damage, nuclear trafficked AREG:prelamin A might alter nuclear prelamin A. To test this we transfected cells with nuclear lamina targeted AREG with a C-terminal 11 amino acid deletion (AREGΔC11) previously shown to promote a global increase in heterochromatin [8]. We constructed a lentivirus expressing AREGΔC11 and infected MECs with this virus or a control-GFP-V5 virus. IF was then performed to detect AREG

and prelamin A using an antibody specific for the amino acids C-terminal to the cleavage site for ZMPSTE24 (clone PL-1C7). In MECs expressing GFP, low levels of AREG and scarce, heterogeneously distributed prelamin A were detected. High levels of AREGΔC11-V5 expression corresponded to strong perinuclear AREG staining and prelamin A was readily detected at the nuclear periphery and nucleoplasm (Figure 3F). Note that anti-V5 and prelamin A antibodies are mouse monoclonals precluding direct anti-V5 detection. A 3D image of the z-stacks is shown below. White arrows indicate cells with strong nuclear AREG and prelamin A IF organized in a perinuclear manner. The green arrow indicates two cells with increased size (likely S/G2) with AREG distributed in a perinuclear location. This is accompanied by increased prelamin A including some large foci, consistent with AREG mediated accumulation of prelamin A. The blue arrow indicates a cell without detectable AREG containing randomly distributed prelamin A. Prelamin A was significantly co-localized with AREG (Figure 3G). Together these results support the hypothesis that RS induces AREG-dependent increases in nuclear prelamin A to the nucleus. Prelamin also interacts with HP1α [60] and SUV39h1 and HP1α may undergo reciprocal stabilization [61]. The immunoblot in Figure 3H shows that cells infected with lenti-AREGΔC11-V5 expressed an increased level of HP1α and SUV39h1 protein compared with control GFP accompanied by an increase in H3K9me3.

To further examine the effects of RS on nuclear prelamin A, we tested the effect of HU on prelamin A incorporation into the NM in untransfected MECs. Figure 3I shows that, in most cells, prelamin A was not detected or weakly detected in the nuclear lamina indicated by lamin B in untreated cells. In contrast, HU resulted a majority of cells with prelamin A colocalized to the NM with lamin B.

To determine the effect of AREG depletion, MECs transfected with siNT or siAREG were used for prelamin A and AREG IF. Prelamin A was detected at the NM of some siNT-transfected cells while in other cells it was colocalized with AREG at least partially in the cytoplasm/ER. A subset of cells were devoid of detectable prelamin A. HU stimulated an increase in nuclear rim associated AREG and prelamin A (Figure 3J). In contrast, prelamin A immunostaining in MECs depleted of AREG was weaker and appeared mostly localized to the cytoplasm/ER and HU did not increase detection of prelamin A or NM localization.

Consistent with the reduction in H3K9me3, immunoblot analysis of HP1α and SUV39h1 proteins in siAREG-transfected MECs showed that reduction of AREG decreased HP1α and SUV39h1 (Figure 3K).

Heterochromatin bound HP1α has been proposed to form collapsed globules which achieve segregation of heterochromatin domains [62]. Such structures may form the HP1α puncta that are associated with dense domains of heterochromatin called chromocenters [63]. Consistent with reduction of HP1α, large HP1α-marked chromocenter foci were significantly reduced by AREG depletion (Figures 3L, 3M).

Together these observations are consistent with rapid nuclear AREG trafficking response to RS that increases nuclear prelamin A and transiently enhances global H3K9me3.

Loss of endogenous AREG results in genomic instability. Both the presence of heterochromatin and loss of heterochromatin present challenges to DNA repair and replication. Therefore, we next investigated the effects of AREG KD on DNA damage in *BRCA2*$^{mut/+}$ MECs. As a consequence of BRCA2-haploinsufficiency [64] these cells are expected to demonstrate suboptimal fork protection resulting in single-strand and DSBs due to resection of ssDNA at stalled forks [38]. We therefore evaluated the effect of AREG depletion on DNA breaks (SSBs and DSBs) using alkaline comet assays on both normal and *BRCA2*$^{mut/+}$ MECs. The results shown in Figures 4A, 4B indicate that, as expected, the Olive tail moment was increased by HU in normal MECs, while more frequent and extensive DNA damage was evident in *BRCA2*$^{mut/+}$ MECs. AREG depletion alone also resulted in a small but significant increase in DNA breaks in normal MECs and the absence of AREG had no further effect. In contrast, in *BRCA2*$^{mut/+}$ MECs, AREG depletion resulted in a significant induction of DNA breaks that was further amplified following HU treatment. These results indicate that endogenous AREG attenuates RS-induced DNA damage in *BRCA2*$^{mut/+}$ MECs. Since *BRCA2*$^{mut/+}$ MECs were highly sensitive to loss of AREG and RS, we investigated the effect of AREG depletion specifically on DSBs using a neutral comet assay. A significant increase in DSBs in both control and HU-treated AREG-depleted *BRCA2*$^{mut/+}$ MECs relative to control in the presence or absence of HU was obtained (Figures 4C, 4D). Thus, AREG depletion in *BRCA2*$^{mut/+}$ MECs results in genomic instability involving DSBs that is exacerbated by exogenous RS.

Immunoblot analysis of several DNA damage response proteins revealed activation of P-ser1981ATM following HU in siNT-transfected *BRCA2*$^{mut/+}$ MECs that was enhanced following siAREG-transfection (Figure 4E). A low but reproducible increase in P-ATM (*Figure S2*) was also observed in AREG-depleted cells without HU treatment indicative of dsDNA breaks. As expected, the ATR substrate, P-CHK1 was strongly phosphorylated in HU-treated MECs. P-CHK1 was not detected in siNT-transfected MECs, but was evident in siAREG-transfected MECs even in the absence of HU indicating an RS response in these cells.

Heterochromatin plays key a role in the localized rapid response to RS. An ATR-regulated cascade of chromatin modification involves G9a and SUV39h1 which catalyze transient heterochromatin assembly specifically at stressed replication forks. This is thought to be important for establishing a local environment for the recruitment of several fork stabilization factors [65]. Given the effect of nuclear-translocated AREG KD on global heterochromatin, we reasoned that AREG KD might impair the transient formation of H3K9me3 at stalled replication forks resulting in increased fork collapse. To investigate this, we performed a proximity ligation assay in *BRCA2*$^{mut/+}$ MECs 72hrs after siAREG or siNT infection treated with HU for 2h. Nascent DNA was labeled with iodo-deoxyuridine (IdU) followed by incubation with mouse anti-BrdU and rabbit anti-H3K9me3. Proximal antibodies were detected with secondary oligo-coupled antibodies and visualized by rolling circle amplification with Alexa564-labelled nucleotides. While untreated/siNT transfected *BRCA2*$^{mut/+}$ MECs exhibit a low but detectable level of BrdU:H3K9me3 proximal foci, as anticipated, HU treatment resulted in a significant increase in focus formation (Figures 4F, 4G). Consistent with fork stalling, AREG KD alone resulted in an increase in foci above control levels. Compared to control HU-treated MECs, significantly greater foci numbers were detected in AREG KD MECs following HU treatment.

Together these results indicate that, although transient local formation of heterochromatin at stalled forks is not compromised in AREG-depleted *BRCA2*$^{mut/+}$ MECs, these cells experience increased DSBs likely due to collapsed forks.

Endogenous AREG depletion increases new replication origins and firing of multiple origins. Since the transient H3K9me3 stalled fork protection mechanism appeared unaffected by AREG knockdown, we sought to determine if there was an impact on DNA replication. To understand the etiology of the increased DNA damage we observed in AREG-depleted *BRCA2*$^{mut/+}$ MECs, we

employed DNA fiber assays. Cells transfected with siNT or siAREG were incubated sequentially with the thymidine analogues CldU followed by IdU for 20 minutes each. A small but significant decrease in CldU:IdU ratio was observed after AREG KD which may be consistent with slowing of the fork during progression in these cells. To address the effect of AREG depletion on strand resection, some cultures were treated with HU for 4hr immediately after IdU washout. This resulted in strand resection in both siNT and siAREG transfected MECs, however this was significantly greater in siAREG-depleted MECs (Figures 5A, 5B). Fork regression was prevented by the co-treatment with the MRE11 inhibitor, mirin, although protection was incomplete in siAREG-transfected MECs. This may be attributed to an increased frequency of fork collapse in the AREG KD MECs. Slowing of the replication fork can result in activation of normally dormant replication origins [66]. Notably, DNA fiber lengths were significantly shorter in untreated siAREG-transfected MECs compared with control MECs indicating a slowed replication rate (Figure 5C). Collapsed forks resulting in restart of new origins as indicated by IdU-only labeled fibers were also significantly more frequent in AREG-depleted MECs as indicated in the graph and example image (Figure 5D). No changes between treatment groups in bidirectional forks were observed (not shown), however AREG KD resulted in a significantly greater number of fibers with CldU-IdU-CldU-IdU-labeling indicative of multiple origins of replication within a single strand (Figures 5E, 5F).

Aberrant origin activation and normal timing of replication could result in nucleotide depletion thereby promoting RS and DNA damage in *BRCA2*$^{mut/+}$ MECs. In support of this, supplementation of media with nucleosides significantly reduced P-H2AX foci accumulation following AREG KD (Figures 5G, 5H). Using a neutral comet assay, we also tested the effect of nucleotide supplementation directly on DSB formation following RS induced by a 24hr treatment with aphidicolin. Figure 5I indicates a significant increase in DSBs in siAREG-transfected *BRCA2*$^{mut/+}$ MECs compared to normal MECs. Similar to HU-induced RS, a 20h culture with aphidicolin increased DSBs significantly more in AREG KD compared to control MECs. Again, consistent with a role for nucleotide depletion in these cells, nucleoside supplementation for 48 hrs markedly reduced the Olive tail moment in AREG KD but had no effect on siNT-transfected MECs. Reduced constitutive heterochromatin might increase global transcription levels. To examine this we cultured siNT and siAREG-transfected MECs in the presence of BrU for 20 min followed by IF

detection with anti-BrdU. IF and analysis in Fiji (**J** and **K respectively**) show that the level of transcription increased significantly by approximately 2-fold.

In total, these results are consistent with large scale reduction in constitutive heterochromatin resulting in dysregulation of replication, enhancing replication stress and increased genomic instability in AREG-depleted MECs.

Absence of AREG in BRCA2$^{mut/+}$ MECs disrupts the Ran-GTPase gradient and increases nuclear membrane invaginations: The association of AREG with lamin A and reduction of H3K9me3 and heterochromatin compaction after AREG depletion suggested that the effects of depletion might impact the NM. Heterochromatin was found to be essential for maintaining the Ran gradient and the nuclear import of ATM in fibroblasts from Hutchinson-Gilford progeria syndrome patients [67]. The ratio of nuclear to cytoplasmic Ran is typically 3:1. Ran IF in siNT-transfected control MECs in AREG KD MECs revealed the normal nuclear-cytoplasmic distribution. However, a profound reduction of the Ran gradient was observed in AREG KD *BRCA2*$^{mut/+}$ (Figures 6A, 6B). Nuclear localization of 53BP1 is dependent on active transport mediated by Ran-GTPase-importin α/β-mediated nuclear import [68]. Consistent with their BRCA2-deficient status, we found that unperturbed *BRCA2*$^{mut/+}$ MECs also contained nuclear 53BP1 foci (Figures 6A). Although, loss of endogenous AREG significantly decreased 53BP1 foci (Figure 6A, 6C). Given the disruption of the Ran gradient, we next investigated whether reduced nuclear foci might be a consequence of altered 53BP1 subcellular localization. Immunoblot of cytoplasmic and nuclear fractions of control and AREG-depleted *BRCA2*$^{mut/+}$ MECs revealed cytoplasmic 53BP1 in both siNT and siAREG transfected MECs (Figure 6D). 53BP1 is sumoylated in response to DNA damage [69] and high molecular weight forms were increased in response to either AREG KD and/or HU treatment. However, nuclear 53BP1 protein levels were consistently lower in AREG-depleted MECs regardless of HU-induced RS. As in Figure 1, the 23kDa and 18kDa nuclear AREG peptides were increased by HU treatment.

ATM and ATR proteins also require Ran-GTPase facilitated nuclear transport through the nuclear pore. AREG depletion similarly reduced the nuclear content of ATM and to a lesser extent, ATR (Figure 6E). The *BRCA2* $^{+/6872del4}$ truncating mutation in these cells lacks an NLS [70,71] which would prevent at least 50% of BRCA2 nuclear import in these cells, however we either did not detect BRCA2 (Figure 6D) in the nuclear or cytoplasmic fractions of these MECs. In contrast,

AREG KD did not impact the nuclear content of the small nuclear proteins RBM22 (pre-mRNA splicing) and DDX52 (RNA helicase). Thus, in addition to replication dysregulation due to H3K9me3 reduction in AREG-depleted MECs, the reduced Ran gradient and import of DNA repair proteins could also negatively impact on genome repair capacity.

Heterochromatin interactions with the nuclear lamina and nuclear pore complexes maintain its peripheral localization [72]. Since KD of AREG reduces H3K9me3 heterochromatin and disrupts the Ran gradient and nuclear import in AREG-depleted MECs, we next looked to see if NPC distribution was altered in these cells. The images in Figure 6E show the primarily uniform nuclear rim staining in control-transfected MECs with mAb414 which recognizes FG repeat nucleoporins (Nups). AREG depletion resulted a reduction in nuclear rim Nup IF and introduced regions of discontinuity. In addition, these cells demonstrated increased nucleoplasmic Nup distribution. Both blockage of lamin farnesylation (which reduces lamin A incorporation into the nuclear matrix) and accumulation of farnesylated lamin A can increase the formation of nuclear invaginations known as nucleoplasmic reticulum (NR) [73]. To assess this we rendered 3D images of Z-stacks of MECs immunostained with mAb414 following siNT or siAREG transfection. Figure 6F shows that nucleoplasmic Nups in AREG-depleted MECs are at least partially associated with increased NR formation. In a subset of transfections NR invaginations were large enough to be detected following deconvolution of z-stacks of lamin A/C IF (*Figure S3)*.

AREG contributes to nuclear membrane integrity and prevents senescence: RS can lead to accumulation of cytosolic DNA activating the cGAS/STING cytosolic DNA sensing pathway activating IFN responses [74] and has been implicated in both neoplasia [75] and senescence [76]. Analysis of the incidence of NM ruptures and blebbing following AREG KD and rupture from *BRCA2*$^{mut/+}$ MECs showed increased incidence that was not further increased upon HU-induced RS (Figures 7A, 7B). Although infrequent, we also noted anaphase bridges in AREG-depleted but not control MECs (panel v). H3K9 KMT-deficient MEF cells display activation of IFN signaling, including overexpression of type I IFN regulators Irf7, Irf9, and Stat1 [77,78]. cGAS colocalized with cytosolic DNA in AREG-depleted MECs which also resulted in the activation of several genes in the innate immune pathway tested including robust upregulation of Stat1 (Figure 7C).

DNA damage as a consequence of RS and activation of AREG-depleted MECs might be expected to promote senescence. To test this possibility, siAREG-transfected *BRCA2*$^{mut/+}$ MECs were treated acutely with HU to generate RS and DNA damage followed by wash-out of HU.

Compared to controls increased percentages of senescence-associated (SA)β-gal positive cells were evident in even in untreated MECs by day 5 after treatment that was not-significantly increased by prior treatment with HU (Figure 7D, 7E).

Chronic replication stress induces nuclear AREG and expression of FOXM1and ERα-correlations in mammary tissue: Our data show that AREG is important for maintaining H3K9me3 in MECs and that AREG nuclear translocation in response to RS helps to prevent DNA damage, most prominently in *BRCA2*$^{mut/+}$ MECs. MECs are subject to multiple rounds of replication stress over a lifetime and *BRCA2*$^{mut/+}$ MECs are at high risk for eventual transformation resulting predominantly in estrogen receptor (ER)$^{+}$ luminal B breast cancers. Aside from effects on heterochromatin, the AREG C-terminal domain and proAREG but not the ectodomain were shown to increase the mitotic genes Forkhead Box M1 (FOXM1) and MYBL2 in keratinocytes [79]. Notably, the *ESR1* gene encoding ERα is an important FOXM1 target gene [80]. qPCR to detect AREG, FOXM1 and ERα transcripts following 5 days of chronic RS in 15uM HU showed a marked increase in all three mRNAs in the *BRCA2*$^{mut/+}$ MECs (Figure 8A). Similar to acute HU-induced RS, immunoblot confirmed the increase in 23kDa and 18kDa AREG peptides as well as FOXM1 and ERα protein expression (Figure 8B). We predicted that loss of BRCA2 resulting in DNA damage and or conditions with potential for replication stress *in vivo* would result in increased nuclear AREG. Six-week old MMTV-cre;*Brca2*$^{+/+}$; *Brca2*$^{f/+}$ and *Brca2*$^{f/f}$ mice were used for immunohistochemical (IHC) analysis of AREG. Mammary epithelium from both wt and *Brca2*$^{f/+}$ mice did not show significant differences although prominent nuclear AREG staining was present in *Brca2*$^{f/f}$ mammary glands, possibly due to chronic RS (Figure 8C). We next examined mammary sections from non-carrier and *BRCA2*$^{mut/+}$ patient samples. AREG was present in low-moderate levels in epithelium from non-carriers (Figure 8D (i-iii)). Similar to mice, regions of *BRCA2*$^{mut/+}$ histologically normal tissue expressed similar levels of AREG as controls, although some regions including both lobules and ducts were strongly positive for nuclear AREG (Figure 8D (iv-vi). Breast tissue from *BRCA1/2* carriers is characterized by increased incidence of hyperplastic and often premalignant lesions [81,82]. Accordingly, we found regions of dysplastic and overt hyperplastic regions in *BRCA2*$^{mut/+}$ patients. Although the majority of cells were negative for nuclear AREG, dysplastic/hyperplastic lesions were invariably accompanied by intense nuclear localization of AREG in up to 90% of cells (Figure 8D (vii-ix)).

The expression of ERα was found in a small proportion of epithelial cells randomly distributed in ducts and lobules across normal mammary tissue (Figure 8E panels i, ii). Recently it was shown that *BRCA2*$^{mut/+}$ mammary tissue has a distinct pattern of ER expression with regions of contiguous and strong ER expression [83]. In accordance with this we noted more frequent ERα expressing MECs and regions of several adjacent, strongly positive ERα^{+} cells (Figure 8E panels iii, iv). Similar to nuclear AREG, across different samples, the ERα was expressed in the vast majority of cells both within small areas of dysplasia and in larger ductal hyperplasias. Based on our finding that chronic RS induces FOXM1 expression, we also investigated the presence of the protein in non-carrier and *BRCA2*$^{mut/+}$ mammary glands. Figure 8F depicts representative IHC staining of FOXM1 in lobules and ducts. Overall FOXM1 was detected in intermittent cells in ducts and lobules of both non-carrier and *BRCA2*$^{mut/+}$ epithelia (compare panels i, ii and v). Similarly many ducts and lobular units of both normal and *BRCA2*$^{mut/+}$ glands expressed low to undetectable FOXM1 (not shown). Small areas of hyperplasia as in panels iv and viii contained numerous FOXM1^{+} nuclei irrespective of BRCA2 status, while larger regions of hyperplasia showed a reduced proportion of FOXM1^{+} MECs (panel viii) or were negative for FOXM1 (panels iii and vi). Higher proportions of FOXM1^{+} MECs in *BRCA2*$^{mut/+}$ glands tissue may give rise to the increased number of ERα^{+} cells present in *BRCA2*$^{mut/+}$ glands. In contrast, cells in large hyperplastic lesions that expressed little or no nuclear FOXM1may be due to the loss of proliferative activity within limited benign lesions.

Discussion

Repeated exposure to replication stress is thought to contribute significantly to the development of cancer as a consequence of ensuing genomic instability [31,84]. Indeed, the relative frequency of sporadic cancers occurring in breast epithelial cells compared with other tissues is a reflection of continued proliferation and renewal over decades. Supporting this notion, carriers of deleterious *BRCA2* mutations deficient in replication fork stabilization and HR are at significant risk of breast and fallopian tube/ovarian cancers [85-87]. Given this, mechanisms that protect *BRCA2*$^{mut/+}$ MECs from genomic instability are likely paramount for reducing chronic DNA damage and resulting senescence within the gland. Here we have demonstrated an unanticipated role for nuclear lamina-association of AREG that contributes to maintenance of heterochromatin and prevents DNA damage in response to RS, critical in *BRCA2*$^{mut/+}$ MECs to prevent the development of senescence.

In turn, nuclear AREG can promote the expression of FOXM1 and ERα expression which then contribute to RS recovery and the expansion of ER^+, potentially precancerous cells.

The formation of transient heterochromatin is an acute response to both DSBs [42] as well as stalled replication forks [65]. Although depletion of AREG reduces global heterochromatin and/or compaction, transient heterochromatin formation at stalled forks appeared unaffected as detected based on proximity ligation analysis of H3K9me3 and IdU-labeled nascent DNA. Thus AREG has a role in maintaining constitutive heterochromatin in MECs which involve regulation of nuclear prelamin A. It is possible that AREG-dependent increase in nuclear prelamin A in association with increased HP1α in response to RS/DNA damage could facilitate the transient long range propagation of heterochromatin which occurs at DSBs [17]. However the rapidity of this response may preclude such a role. In this case increased nuclear AREG and H3K9me3 in response to RS may be more important for avoiding further stress by repressing transcription, slowing replication and/or limiting checkpoint activation. Aside from effects on chromatin, HP1α was reported to promote efficient homologous recombination [88], which is consistent with a nuclear AREG-associated mechanism contributing to RS resistance in *BRCA2*$^{mut/+}$ MECs.

The genomic consequences of the reduced and altered heterochromatin state in AREG KD MECs included increased firing frequency of new and multiple origins and ultimately fork stalling and collapse. We showed that the resulting DNA damage caused by AREG KD was mitigated by nucleotide supplementation. These results are a reflection of the altered chromatin state in the absence of AREG resulting in deregulated replication and underscores the important function of AREG in promoting genomic stability through contributing to heterochromatin maintenance.

The stress kinase p38α provides an important rapid signal in response to DNA damage and we have established that the RS-induced increase in AREG association with early endosomes, AREG processing and H3K9me3 formation are p38 activity-dependent. DNA damage in HeLa cells induces p38 activation-dependent internalization of the EGFR [89] and may traffic via recently described nuclear envelope-associated endosome (NAE) pathway [90]. We found HU treatment significantly increased AREG colocalization with EEA1 positive early endosomes. This could conceivably result in NAE mediated nuclear entry of AREG. Other evidence suggests that after phorbol ester stimulation, AREG undergoes ER retrieval and enters the trans-Golgi network (TGN) followed by entry into nucleus via nuclear pores [8]. The close juxtaposition of AREG and lamin A in cytoplasmic PLA foci after HU suggests a common trafficking pathway. With respect

to this, prelamin A and its assembly into the nuclear envelope are regulated by sorting nexin 6 (SNX6), a component of the retromer which transports transmembrane receptors from endosomes to the trans-Golgi network (TGN) for recycling. SNX6 interacts with lamin A linking it to the outer surface of the ER and is required for lamin A nuclear import occurs across the nuclear pore complex [47]. AREG endosome interaction with prelamin A at the ER surface may account for the significant increase in lamin A:AREG PLA foci in response to RS. Trafficking of AREG via this pathway and/or NAE would contribute to the stabilization of AREG protein during RS due to bypass of the late endosome/lysosomal pathway. Evidence suggests that prelamin A farnesylation, carboxymethylation and cleavage can occur either at the outer surface of the ER, in the nucleus or at the nuclear rim [91]. The accumulation of prelamin A in response to either AREGΔC11 or RS that results in AREG interaction with prelamin A could limit farnesylation at the ER prior to entry into the nucleus thus increasing the nuclear level of prelamin A. Further studies are necessary to resolve this possibility.

While lamin A can interact directly with SUV39h1 to prevent degradation resulting in increased H3K9me3, this interaction is strongly enhanced in the presence of progerin or prelamin A in *zmpste24*$^{-/-}$ mouse cells [30]. Moreover, HP1α associated with the nuclear matrix is markedly increased in *zmpste24*$^{-/-}$ MEFs [60]. Expression of nuclear AREG increased both HP1α and SUV39h1 and as well as the detection of nuclear prelamin A. Thus increased prelamin A association with SUV39h1 (and HP1α associated with SUV39h1) is a candidate mechanism for the increase in these proteins resulting in increased formation of H3K9me3. In contrast, AREG depletion resulted in the accumulation of prelamin A, primarily in the cytoplasm/ER in untreated cells that dissipated after HU treatment.

Our experiments showing that depletion of endogenous AREG reduces H3K9me3 and/or results in heterochromatin decompaction indicates a constitutive function for AREG in the maintenance and/or establishment of heterochromatin in MECs. Positioning heterochromatin at the nuclear periphery occurs in a lamin A/C-dependent manner mediated by PRR14 which interacts with H3K9me3 via HP1 [25]. Thus reduced HP1α would contribute to the loss of peripheral heterochromatin we observed in AREG-depleted MECs. The reduction in endogenous AREG also resulted in major perturbations in NM invagination and the Ran-GTPase gradient. Heterochromatin affects the structural integrity of the nuclear envelope which, when compromised, results in increased membrane invagination [92] and nuclear blebs prone to rupture [93].

Consistent with reduced SUV39h1 levels after AREG KD, inhibition of HMTs and subsequent reduction in heterochromatin also dissipates the Ran gradient resulting in reduced import of large DNA repair proteins including 53BP1 and ATM [67,94]. Nuclear invaginations incorporate regions of high membrane curvature [95]. These regions are prone to nuclear rupture, which reduces the retention of DNA repair factors [96]. Thus loss of the Ran gradient and increased nuclear ruptures would be anticipated to further reduce the repair capacity in MECs contributing to increased DNA breaks. Nonetheless, despite the reduction in nuclear ATM and reduction in 53BP1 foci, we still observed robust activation of ATM and H2AX foci following AREG KD which were increased after HU in AREG-depleted MECs indicative of widespread DNA damage.

NM rupture releasing DNA into the cytoplasmic compartment, likely combined with RS generated cytoplasmic DNA fragments in AREG KD MECs, resulted in robust activation of the IFN-1-like response and development of SA-βgal enzymatic activity. RS is intrinsic to progeroid cells and is associated with the appearance of cytosolic DNA and viral mimicry consisting of activation of the cGAS/STING pathway which promotes the STAT1-regulated IFN-like response [97]. This pathway is involved in enforcing senescence [98] and interestingly, Stat1 functions as a breast cancer tumor suppressor in a mouse model [99]. Thus, by maintaining and increasing heterochromatin in response to RS, nuclear AREG prevents excessive DNA damage. On the other hand, absence of AREG would promote NM dysfunction and activation of the IFN-like response which in turn could suppress tumor formation. Thus, AREG has a fundamental role in enhancement of heterochromatin after RS to prevent excessive DNA damage which is important for continued proliferation of *BRCA2*$^{mut/+}$ MECs that are prone to fork collapse, DSBs and tumorigenesis.

BRCA2$^{mut/+}$ mammary glands, where DNA damage signaling from RS is increased, contain expanded populations of aberrant luminal progenitor cells [100,101]. In particular, mammary glands of carriers of *BRCA2*$^{mut/+}$ mutations were found to contain increased numbers of ERα expressing MECs [101], recapitulated in this study. This is the first report of the association between RS, nuclear AREG and the induction of FOXM1 and ERα in MECs. Studies in hTERT-keratinocytes found that AREG-silencing results in mitotic arrest associated with reduced expression of mitosis-related genes which was restored by proAREG and AREG-C-terminal domain, but not by soluble AREG [102]. AREG KD markedly inhibited the expression of FOXM1 in these cells in a manner that could not be reversed by the addition of exogenous AREG or other EGF ligands implicating intracellular

AREG [79]. FOXM1 cooperates with MYBL2 to transcribe genes necessary for S/G2/M-phase [50] and is transcriptionally active during a DNA-damage-induced G2 arrest and is essential for checkpoint recovery [103]. Aberrant FOXM1 expression is an early event in oncogenesis and has been associated with genomic instability [104]. Moreover, FOXM1 is a target gene for the ERα [105] while, in turn, FOXM1 can activate transcription of the human ESR1 promoter [80]. Importantly, FOXM1 contributes to expansion of the luminal progenitor pool [106]. In keeping with a possible role for RS and subsequent activation of nuclear AREG in expansion of ERα$^+$ MECs, we detected increased FOXM1 and nuclear AREG in regions of mostly ERα expressing dysplastic and hyperplastic cells in breast tissues. These same glands contain a subset of luminal progenitors that can give rise to both ER$^+$ and ER$^-$ progeny considered potential cells of origin for breast cancers that have altered proteostasis in conjunction with enrichment of mTORC1 pathway genes [83]. Notably, AREG was recently shown to be critical for maintaining ERα expression and signaling in acquired aromatase inhibitor resistant breast cancer cells through activation of PI3K/Akt/mTOR signaling and FOXM1 upregulation which function in a feedforward loop to increase ERα signaling [46]. Our results suggest the possibility that this signaling hub may also be at play in mammary progenitor cells subjected to RS which is amplified in *BRCA2*-defective MECs. Thus, chronic RS activates nuclear AREG, increasing FOXM1 expression which may then contribute to expansion of ER+ cells of origin for breast cancer.

Overall this study demonstrates that nuclear AREG has an unanticipated role in maintaining heterochromatin and NM function in MECs. Moreover, nuclear localization of AREG is a novel component of the RS response that provides insight into a mechanism by which *BRCA2*$^{mut/+}$ MECs avoid excessive DNA damage during progenitor cell replication and how RS that leads to DNA damage can promote the expansion of ER$^+$ progenitor cells.

Acknowledgements: This work was funded by Canadian Cancer Society Research Institute grants i2i-18 #705975 and INNOV-18 #705940 to M.AC.P. We thank the University of Ottawa CBIA core for assistance with imaging and image analysis. We are grateful to Cheryl Lewis (UT Southwestern, Texas) for the generous gift of hTERT-mammary cells and Dr. William Muller (McGill University, Quebec) for MMTV-cre mice.

Methods:

Cell culture: hTERT mammary epithelial cells were obtained from Dr. C. Lewis (UT Southwestern, TX and were established as described [107]. Cell are maintained in DMEM/F12 (Wisent, 319-075-CL) containing 0.4% pituitary extract (Gibco, 13028-014), Glutamax (Gibco, 35050-061), amphotericin B, gentamicin, penicillin/streptomycin, supplemented with 5ng/ml EGF, 0.5ug/m hydrocortisone, 5ug/ml insulin, 5mM 3,3,3-tri-iodo-thyronine and 5nM isoproterenol (all Sigma) incubated at 37°C humidified atmosphere under 5% CO_2. For all siRNA transfections, 15nM AREG was added to the medium to obviate EGFR-mediated effects in AREG-depleted MECs. For nucleoside supplementation, EmbryoMax® Nucleosides 100× (ES-008-D, Sigma-Aldrich) were used with 50-fold dilution.

Antibodies

Antibody	Source	Catalogue #
53BP1	Novus Biologicals	NB100304
Actin	Sigma	A-2066
ATM	Calbiochem	PC116
Amphiregulin	Proteintech	AF262
Amphiregulin	Proteintech	16036-1-AP
BRCA2	Abcam	ab27976
BrdU [MoBu-1]	Abcam	ab8039
BU1/75 [ICR1]	Abcam	ab6326
BrdU [B44]	Becton Dickson	347580 (7580)
cGAS	Cell Signaling	79978
CHK1	Cell Signaling	2360
CHK2 (1C12)	Cell Signaling	3440
DDX52	Bethyl Laboratories	A303-053A
EEA1	Cell Signaling	3288
ERα	Santa Cruz	MC-20: sc-542
ERα	Abcam	[EVG F9] (ab19349)
GAPDH	Cell Signaling	97166S
gH2AX	Cell Signaling	2577
H3K9me3	Thermo	PA5-31910
HP1α	Sigma	05-689
Lamin A/C	SantaCruz	sc-7292
Lamin A/C	Cell Signaling	2032
Mab 414	Biolegend	902901
P-ser1981 ATM	Calbiochem	DR1002

p38 MAPK	Cell Signaling	9212
phospho-p38	Cell Signaling	D3F9
P-thr68 CHK2	Thermo	PA5-17818
P-ser345 CHK1	Cell Signaling	2348
Prelamin A (PL-1C7)	Millipore Sigma	MABT858
RAN	Millipore	07-517
SUV39h1	ProteinTech	10574-1-AP
Vinculin	Abcam	ab129002
V5-Tag	Abcam	AB27671
Secondary antibodies	**Source**	**Catalogue#**
Rabbit IgG (HRP-linked)	Cell Signaling	7074S
Mouse IgG (HRP-linked)	Cell Signaling	7076
Goat IgG (HRP-linked)	Invitrogen	A15999

qRT-PCR: Cells were lysed after culture and the RNA is extracted using the Aurum™ Total RNA mini kit (BIO-RAD, 732-6820) following the manufacturer's protocol and was resuspended in 40ul of nuclease-free water and stored at -80°C. cDNA was synthesized by reverse transcribing 1ug of RNA with reverse transcriptase (BIO-RAD, 1708891). The resulting cDNA was diluted to 20ng/ul and mixed at 1:10 ratio with the SsoAdvanced Universal SYBR Green Supermix (BIO-RAD, 1725271). The qRT-PCR reactions were performed using the CFX96 Real-Time PCR System [C-1000 Touch Thermal Cycler] (BIO-RAD) and relative gene expressions were calculated using the $\Delta\Delta C_T$ method normalized to S18 housekeeping gene. Primers were designed online using the National Center for Biotechnology Information (https://www.ncbi.nlm.nih.gov/tools/primer-blast/) and manufactured by Invitrogen/ Thermo Fisher. Primer sequences can be found in Supplementary Table 1.

Construction of lenti-AREGΔC11: Lenti-AREG (C-terminal V5 tag) was purchased from GeneCopia (EX-OL00093-LX304).The C-terminal 11 amino acids were deleted using the Q5® Site-Directed Mutagenesis Kit (New England Biolabs, E0554S). Primers were designed using the NEBase Changer tool to generate the deletion were: forward- 3'-TACCCAACTTTCTTGTAC-5' and reverse- 3'-TACCCAACTTTCTTGTAC-5'. Plasmids were verified by sequencing.

Lentivirus production: HEK293T cells were seeded into 10 cm plates and 3 days later the plasmid transfection mix was prepared by combining 240 µL Optimem, 8 µg transfer plasmids, 4

µg PCMV (envelope plasmid), 6 µg pMD2.G (packaging plasmid), and 72 µL PEI (4 µL of PEI/1 µg DNA). The DNA:PEI mixture was gently mixed for 20 minutes at room temperature, then diluted to a total volume of 3 mL with Optimem media. The mixture was then added onto cells. The following day (D4), Optimem was removed and replaced with 10 mL of fresh media (DMEM +10%FBS). At 48h and 72h post infection, media containing virus were obtained and stored at 4°C. A virus precipitation kit (Benchmark bioscience) was used to concentrate and store the lentivirus.

siRNA reverse transfection: hTERT-MECs were grown for 72h before transfection to ensure optimal growth period. On the day of transfection, a mixture of siRNA (Dharmacon ON-TARGETplus SMART Pool human AREG siRNA or Non-targeting pool, Horizon (D-001810-10-05) and transfection reagent (Dharmacon T-2001-01) was made by diluting with hTERT media. The mixture was then incubated in 37°C for 20 mins. The hTERT-MECs were then trypsinized, collected, and combined with the transfection mixture. The cell number was adjusted according to the company's protocol. hTERT-MECs were transfected for ~60h before switching into fresh media for 12 hours prior to harvest or treatments.

DNA comet assays: Assays were performed as described in neutral conditions and alkaline conditions doi: 10.21769/BioProtoc.915][108 109] [doi:10.1007/978-1-0716-2433-3_7.) Microscope slides were coated with 1% NMP agarose (FroggoBio, A87-500G). Prepared slides were let cooled at room temperature overnight. The next day, cells were trypsinized and collected in PBS on ice. 1% LMP agarose (Bio-Rad, 161-3111) kept at 37°C was mixed with collected cells at ~1000 cells/ul. Around 75ul of cell mixture was dispensed onto the coated slides and flattened with a coverslip. The slides were then let chilled on ice to allow the agarose to harden. Subsequently, another layer of LMP agarose was coated onto the sample. Coverslip is then removed and slides containing the cells were placed into lysis buffer (2.5M NaCl, 100mM EDTA, 10mM Tris-base, pH 10, in ddH2O) at 4°C for at least 1h. The following day, slides were carefully washed with Tris buffer (0.4M Tris, pH 7.4, in ddH2O) before placing into electrophoresis chamber. For alkaline comet assay, electrophoresis buffer was made using 10N NaOH and 200mM EDTA at pH 13. For Neutral comet assay, electrophoresis buffer was made using 300mM sodium acetate and 100 mM Tris-HCl at pH 8.3. Voltage was set to ~0.74 V/cm of chamber length and electrophoresis was performed. SYBR GOLD staining (labels ssDNA and dsDNA) was performed and slides

containing the gel was let dry before immediately imaging. A neutralization (0.4M Tris, pH 7.4, in ddH2O) washing step was performed prior to akaline comet assay staining. Tail moments were calculated using the OpenComet plugin in Fiji (https://cometbio.org/).

DNA fiber assay: Assays were performed essentially as described [110]. Thymidine analogs solution: 2.5 mM 5-chloro-2′-deoxyuridine (CldU) stock solution and 2.5 mM 5-iodo-2′-deoxyuridine (IdU stock solution were prepared in DMEM/F12. CldU was vortex at room temperature until dissolved and IdU was vortexed after incubated at 60°C. All analogs were aliquoted and stored at -20°C until used. Cells were plated in 6-well plate at 300,000 cells per well and treated with siAREG and siNT for 72h. CldU and IdU were mixed with hTERT media at 25uM and 250uM respectively and incubated for 20min each. HU (5mM) was added subsequently to CldU or IdU to investigate its effect on fork restart and protection, respectively. After incubation, cells were trypsinized with TrypLE and centrifuged for collection. Each sample was then resuspended in ice-cold 1XPBS at 500,000 cells/ml and 2ul of cell suspension was spotted on the silane-coated slide (Sigma-Aldrich, S4651). After 5mins of room temperature incubation, lysis buffer (31.52mg/ml Tris hydrochloride, 14.6mg/ml disodium EDTA, 5mg/ml SDS in ddH2O) was added onto the cell suspension and incubated for another 10mins at room temperature. The slides were then tilted at 25° to 40° to allow the suspension to run down (estimated 5mins); the suspension was air-dried completely. The slides were fixed with 3:1 methanol/acetic acid fixature at -20°C for 15mins and incubated in 70% ethanol at 4°C overnight. The next day, the slides were incubated in 2.5M HCl at 37°C for 1h, washed with 1XPBS, and then blocked with 0.5% BSA in 1XPBS for 30mins. The slides were then incubated with 1:300 monoclonal anti-BrdU antibody [BU1/75 (ICR1)] (Abcam, ab6326) and 1:300 Mouse monoclonal anti-BrdU antibody (clone B44) (Becton Dickson, 347580 (7580)). The slides were then fixed with 4%PFA in room temperature for 15mins and washed with 1XPBS. Next, the slides were incubated with 1:400 Alexa Fluor 555 goat anti−rat IgG (Thermo Fisher Scientific, A21434) and 1:400 Alexa Fluor 488 F (ab′)2 goat anti−mouse IgG (Thermo Fisher Scientific, A-11017). These slides were washed with 1X PBS and mounted with Vectashield plus antifade mounting medium (Biolynx, VECTH19002) for imaging.

Immunofluorescence/Immunohistochemistry: Immunofluorescence was performed with paraffin sections and fixed hTERT-MECs. Cells were fixed with 4% PFA for 15mins at room temperature whereas paraffin sections were pre-fixed and mounted onto microscope slides. Both

type of samples were incubated with a blocking solution (5% BSA, 0.5% Triton-X in 1X PBS) at room temperature for 1 hour. Antibodies were diluted using dilution buffer (1% BSA. 0.1% Triton-X in 1X PBS). Samples were incubated with primary antibodies at 4°C overnight followed by 3 × 5 min PBS wash. Sections were then incubated with secondary antibodies at RT for 1h. Subsequently, the samples were washed again with 1X PBS and counterstained with DAPI (Thermo Fisher Scientific, R37606) for 10 mins before mounting with antifade mounting media (Vector laboratory, Vectashield H1900).

Immunohistochemistry was performed using paraffin sections. After the slides were deparaffinized, they were incubated with 3% H2O2 at room temperature for 20 mins. After 3 x 5 mins PBS wash, the slides were incubated with a blocking solution (DAKO, X0909). Antibodies were diluted using dilution buffer (DAKO, S0809) to working concentrations and applied for overnight incubation at 4°C. The slides were washed 3 × 5 min PBS the following day and HRP-anti-rabbit was applied onto the samples and incubated at room temperature for 1h. After Incubation, DAB working solution was prepared (DAKO, K346711). Application of DAB was time sensitive and a close monitoring under the microscope was needed for the development of a brown colour. Subsequently, the slides were washed and counterstained with hematoxylin (Abcam, ab245880). Dehydration was performed in 70%, 95% and 100% ethanol followed by toluene. Finally, the slides were mounted with coverslips using permanent mounting media (Permount, ThermoFisher).

Proximity Ligation Assay (PLA): hTERT-MECs were fixed with 4% paraformaldehyde (PFA) for 15 minutes at room temperature and then washed 3 x 5mins with PBS. hTERT-MECs were permeabilized 0.3% Triton-X 100 in PBS for 30 minutes. After washing with buffer A (Millipore, DUO82049), the cells were blocked with provided blocking solution (Millipore, DUO82007) for 1 hour at room temperature. Primary antibodies of interest were diluted in Duolink antibody diluent (Millipore, DUO82008) and incubated with the cells at room temperature for 1h or alternatively overnight at 4°C. Subsequently, cells were washed 3x5mins with buffer A before incubation with PLA anti-rabbit PLUS (Millipore, DUO92002) and anti-mouse MINUS probes (Millipore, DUO92004) at 37°C for 1 hour. After washing off the unbound probes, ligation was performed using the ligation kit (Millipore, DUO92008) at 37°C for 30 minutes, allowing the formation of circular DNA templates if the primary antibodies targeting the proteins of interests were in close

proximity. This was followed by the addition of polymerase which amplifies and adds the fluorescently labelled, complementary oligonucleotide probes. Finally, cells were counterstained with DAPI for 10 minutes and mounted with antifade mounting medium for imaging.

Senescence associated β-galactosidase detection: Detection of SAβ-gal was performed as described by Itahana et al PMID: **17634571** for cultured cells.

Western blot: Cells were lysed using RIPA buffer (50 mM Tris-HCl, pH 7.4, 0.1% sodium deoxycholate, 1 mM EDTA, 140 mM NaCl, 1% Triton-X, 0.1% SDS), and total cell lysates were collected prior to the addition of Laemmli buffer (Bio-Rad, #1610747). Protein samples were denatured at 95°C for 5 minutes before running on an 8–12% acrylamide gel. Proteins were transferred to a PVDF membrane for subsequent probing. Specific proteins were detected using the appropriate primary antibodies and horseradish peroxidase-conjugated secondary antibodies (see antibody list). Protein bands were visualized using the Chemiluminescent Substrate ECL (Thermo Fisher Scientific) and imaged on a ChemiDoc MP Imaging System (Bio-Rad).

Mice: FVB/N MMTV-cre Brca2 floxed mice (Jackson Labs) were bred with FVB/N MMTV-cre mice (the gift of Dr. William Muller) to produce Brca2+/+, +/-, -/- genotypes. Euthansia is performed subsequently to describe treatment and mammary glands were harvested for paraffin embedding and RNA extraction. Genotyping of FVB/N MMTV-cre; Brca2 floxed mice ear punch DNA was performed using forward and reverse primers: GGCTGTCTTAGAACTTAGGCTG and CTCCACACATACATCATGTGTC respectively for Brca2, GGGATTGCTTATAACACCCTGTTACG and TATTCGGATCATCAGCTACACCAGAG respectively for Cre. Animals were housed on a protocol approved by the University of Ottawa Animal Care and Veterinary Services Committee and in accordance with Canadian Council on Animal Care guidelines. Mammary glands were isolated immediately after euthanasia. Samples were fixed in 10% formalin at 4°C for 24h. Fixed samples were transferred in 70% EtOH to University of Ottawa Department of Pathology and Laboratory Medicine for paraffin embedding and sectioning.

Patient samples: Human breast tissue samples were harvested from prophylactic mastectomy tissue from patients harbouring a germline BRCA2 mutation confirmed by the Children's Hospital of Eastern Ontario Genetics Diagnostics Lab. Non-carrier tissue was obtained from reduction

mammoplasty surgery. Tissue collection was approved by REB with the Ottawa Hospital Ethics Board. Tissues were collected at surgery in collection media (DMEM/F12) and fixed in 10% formalin at 4°C for 72h. Fixed tissues were transferred in 70% EtOH and delivered to University of Ottawa Department of Pathology and Laboratory Medicine for paraffin embedding and sectioning.

Microscopy: Fluorescence imaging was performed with a Zeiss AxioObserver 7-APOllo inverted epifluorescence microscope using a Plan-Apochromat ×63/1.4 oil objective. Images were captured using a Hamamatsu ORCA-Flash LT sCMOS (monochrome) camera and ZEN 3.1 pro software. Imaging of IHC was performed with a Thermo Fisher FL Auto 2 (inverted) microscope using 20X, 0.4 NA air objective for general sample visualization. Images were captured using a colour camera and Auto2 software. For specific and detailed sample staining, imaging was performed Zeiss AxioObserver 7-APOllo inverted microscope using a Plan-Apochromat ×63/1.4 oil objective via Zeiss Axiocam 705 Colour camera.

Image analysis: Images were analyzed using Fiji (Image J) open source software or Imaris Image analysis software.

Statistical analysis: Results were expressed as mean ± S.E.M. of a minimum of 100 cells per treatment group. Two-tailed Student's t-test and one-way ANOVA analyses were performed using GraphPad Prism software. A minimum p-value < 0.05 was considered statistically significant.

Figure Legends

Figure 1. Replication stress increases nuclear AREG in MECs. A, Immunofluorescence of AREG and lamin A in *BRCA2*$^{mut/+}$ MECs treated with vehicle and 4mM HU for 4h. The boxed area is magnified on the right panel showing overlap in IF intensity for AREG and lamin A at regions along the nuclear membrane. **B,** Immunoblot for AREG in *BRCA2*$^{mut/+}$ and normal human hTERT-MECs treated with vehicle (H_2O) or 4mM HU for 4 h (HU), followed by replacement of fresh media without HU and collection at 3h and 18h. **C,** Graph of qPCR of AREG mRNA in untreated, HU-treated and MECs 3h after washout of HU. Bars are S.E.M. of 2 independent experiments in triplicate. **D,** Immunoblot of nuclear and cytoplasmic fractions from MECs transfected with siAREG or the siNT control. 72hrs after transfection MECs were treated

with vehicle or 4mM HU for 4h and harvested then lysates probed with antibodies to AREG, lamin A and GAPDH. HE –high exposure of the nuclear 18kDa band.

Figure 2. Replication stress increases cytoplasmic and nuclear AREG:lamin A interaction and AREG association with EEA1-positive endosomes. A, PLA fluorescence analysis of AREG: lamin A interaction in *BRCA2*$^{mut/+}$ MECs treated with vehicle or HU for 4h. Images were acquired on a Zeiss AxioObserver-7 microscope and rendered in 3D images using Zeiss Zen Blue software (35 z-stacks). A single antibody control is also shown. **B,** Analysis of foci numbers per nucleus corrected for single antibody foci were calculated using Imaris software. Data represent analysis of 100 nuclei per condition. **** p<.0001; *p<.01 (one-way ANOVA). **C,** Dual IF for AREG and EEA1 on BRCA2$^{mut/+}$ and normal MECs treated with vehicle or 4mM HU. Bars are 20μm. **D,** Graph depicting Imaris analysis of colocalization of EEA1 and AREG. Data represent analysis of >100 cells per group. **p<.001 two-tailed t-test. **E,** Immunoblot showing that HU-induced RS differentially activates P-p38α in BRCA2$^{mut/+}$ MECs compared to normal MECs. **F,** Immunoblot of lysates of BRCA2$^{mut/+}$ MECs treated for 4h with vehicle, 10μM SB208530, 4mM HU or 4mM HU with 10μM SB and probed with antibodies for AREG, P-p38α and total p38α. **G,** Representative IF of EEA1 location in cells treated as indicated in F. Bars are 20μm.

Figure 3. Replication stress and nuclear transport of AREG promote H3K9me3 increase nuclear prelamin A residence. A, Representative immunoblot analysis (n=4) of AREG and H3K9me3 and histone H3 in *BRCA2*$^{mut/+}$ MECs treated with vehicle or HU for 4h. **B,** Confocal images of H3K9me3 IF and DAPI in BRCA2$^{mut/+}$ MECs 72h following transfection with siNT control or siAREG and treated with vehicle or HU for 4hrs. Bars are 10 μm. **C,** Graph of H3K9me3 mean fluorescence intensity showing the reduction following AREG depletion. n=200 nuclei/ ****p<.0001; two-tailed t-test. **D,** Graph showing reduction of perinuclear H3K9me3 as assessed by distance of H3K9me3 IF from DAPI-defined perimeter performed using Fiji (n=100 cells/** p<.01). **E,** 3D Imaris rendering of H3K9me3/DAPI in cells treated as indicated. **F,** AREG and prelamin A IF of MECs infected with lenti-GFP-V5 or lenti-AREGΔ11. Bars are 10um. **G,** Graph indicating a significant increase in AREG colocalization with prelamin A following lenti-AREGΔ11 infection (***p<.001; two-tailed t-test). **H,** Immunoblot of MECs

infected as in F to detect AREG, V5, HP1α, SUV39h1, H3K9me3 and H3. Anti-GAPDH was used to control for protein loading. **I,** MECs were treated with or without 4mM HU for 4hrs and IF for prelamin A and lamin B was performed. Magnified regions of boxed areas i and ii are shown on the right. Bars are 20µm. **J,** *BRCA2*$^{mut/+}$ MECs were transfected with siNT or siAREG and 72hr later were treated as in I and IF for AREG and prelamin A was performed. **K,** Immunoblot for AREG, HP1α and SUV389h1 in normal and *BRCA2*$^{mut/+}$ MECs. Protein loading was controlled using anti-GAPDH. **L**, IF of HP1α chromocentres in siNT- and siAREG-transfected MECs. **M,** HPα marked chromocenters defined as foci of >0.5µm were quantified using Fiji software. Bars are 20um. (n=100 cells per group/****p<.0001; two-tailed t-test.)

Figure 4. Depletion of AREG promotes genomic instability with or without exogenous replication stress but does not affect H3K9me3 formation at stalled forks. A, Representative images of comet tails from nuclei within the indicated treatment groups for normal and BRCA2mut/+ MECs. *BRCA2*$^{mut/+}$ and normal MECs were transfected with siNT or siAREG and 72h later treated with vehicle or 4mM HU (4h) and subjected to an alkaline comet assay to detect ssDNA and dsDNA breaks as detailed in Methods. **B,** Graphs depict tail moments (n=50) calculated using the OpenComet plugin in Fiji (https://cometbio.org/). *p<.05; **p<.01; ***p<.001; ****p<.0001 One-way ANOVA. **C,** Representative images of electrophoresed nuclei in neutral conditions. **D,** Graph of tail moment derived from neutral comet assays representing DSBs in BRCA2$^{mut/+}$ nuclei transfected and treated as in A. **p<.01; ****p<.0001; One-way ANOVA. **E,** Immunoblot analysis of DNA damage response proteins in siNT or siAREG transfected MECs treated with vehicle or 4mM HU for 4hrs. GAPDH and vinculin proteins were used as loading controls for low and high percentage PAGE. **F,** Representative nuclei from a PLA assay of H3K9me3:IdU-labelled replication forks in BRCA2$^{mut/+}$ MECs transfected as indicated and treated with HU for 2h. DNA was labeled with IdU for the final 20 minutes of HU treatment and a kit used for proximity ligation reactions conducted after incubation with anti-H3K9me3 and anti-BrdU according to the manufacturer's instructions as detailed in Methods. **G,** Graph depicting PLA foci number per nucleus enumerated using Fiji. ***p<.001; ****p<.0001 One-way ANOVA.

Figure 5. Endogenous AREG promotes fork stabilization and regulates replication fork progression. DNA fiber assays were performed on BRCA2$^{mut/+}$ MECs transfected with siNT or siAREG. Cells were incubated sequentially with the thymidine analogues CldU followed by IdU for 20 minutes in the presence of exogenous AREG. Some cultures were treated with HU for 4h immediately after IdU washout. **A,** CldU (red) and IdU (green) tract lengths were measured and the IdU:CldU ratio calculated (100 tracts per group). Relative to siNT transfected MECs, siAREG-transfection resulted in a significant decrease in tract length after HU treatment indicating nucleolytic degradation of ssDNA. Fork degradation was prevented by the co-treatment with the MRE11 inhibitor mirin in control MECs but only partially inhibited in AREG-depleted MECs suggesting fork collapse. *p<.05; ***p<.001; ****p<.0001 One-way ANOVA. **B,** Representative images of fibers from cells treated as indicated. Bars=2µm. **C,** Fiber lengths were measured and used to calculate replication speed (CldU tract+IdU tract)/2/20min=µm/min) in siAREG and siNT-transfected MECs. ****p<.0001 two-tailed t-test. **D,** Graph shows percentage of new origins indicative of collapsed forks labeled with IdU (green) only (yellow arrow) as indicated in the adjacent image. *p< .05; two-tailed t-test. **E,** Graph showing the percentage of tracts with multiple origins of replication within a single strand labeled with CldU-IdU-CldU-IdU (120 tracts per group). **p<.01; two-tailed t-test. **F,** Representative images of bidirectional forks and tracts with multiple origins of replication in siNT and siAREG transfected MECs (blue arrows) Bars=2µm. **G,** Representative images of P-H2AX foci in MECs transfected with siNT or siAREG in the absence (control) or presence of supplemental nucleoside. **H,** Graph of P-H2AX foci in control and AREG-depleted *BRCA2*$^{mut/+}$ MECs cultured in the presence or absence of supplemental nucleoside. **p<.01; ****p<.0001 One-way ANOVA. **I,** Graph of neutral comet assay tail moments from *BRCA2*$^{mut/+}$ MECs treated for 20h with 0.4 µM APH to induce RS in the presence or absence of nucleoside supplementation to the media. *p<.05; **p<.01; ****p<.0001 One-way ANOVA. **J,** Immunofluorescent detection of BrU to analyze global transcription in siNT and siAREG-transfected MECs treated with or without HU for 4hrs were labeled with BrU for 20 min followed by detection using anti BrdU. Bars are 20µm. **K,** Graph of mean fluorescence intensity of BrU (100 nuclei per group). **p<.01; ****p<.0001; One-way ANOVA.

Figure 6. AREG depletion dissipates the nuclear Ran gradient and promotes nuclear membrane invagination. A, IF of Ran and 53BP1 foci in BRCA2$^{mut/+}$ MECs 72h after transfection with siNT or siAREG. **B,** Graph of mean cytoplasmic to nuclear ratio fluorescence intensity of Ran in MECs transfected as indicated MECs (n=20 cells per treatment group). **C,** Graph depicting 53BP1 foci per nucleus in MECs transfected as indicated and treated with vehicle or 4mM HU for 4h prior to fixation. (n=100 nuclei). B and C; ***p<.001; ****p<.0001 (One-way ANOVA). **D,** Immunoblot of cytoplasmic and nuclear fractions from BRCA2$^{mut/+}$ MECs transfected with siNT or siAREG treated +/- HU probed with anti-53BP1, AREG, lamin A/C and GAPDH. AREG-HE is a high exposure of the lower ~18kDa AREG band in the nuclear fraction. **E,** Immunoblots for the indicated proteins in cytoplasmic and nuclear fractions from siNT and siAREG transfected MECs. Note that high mol wt ATR, ATM and BRCA2 are reduced in nuclei following AREG KD. The AREG peptide band shown is the 23kDa species. **F,** IF of FG nucleoporins in MECs transfected and treated with HU as indicated. Note increasing nucleoplasmic localization in AREG depleted MECs and further enhance by HU. **G,** Imaris rendering of confocal images of siNT and siAREG-transfected MECs immunostained with mAb414 to detect FG nucleoporins (green) counterstained with DAPI (blue).

Figure 7. AREG depletion increases nuclear ruptures resulting in activation of an IFN-like response. A, Graph of percentage of MECs with nuclear ruptures after siNT or siAREG transfection treated with or without HU. Percentages are derived from minimum of 233 nuclei per group and points represent the percentages of nuclei with ruptures calculated from a minimum of 3 microscopic fields from 3 independent experiments. Bars are S.E.M. ***p<.001; **p<.01 One-way ANOVA. **B,** Representative images of DAPI and cGAS immunostained nuclei from (i), siNT transfected MECs and (ii-v), siAREG-transfected MECS. (vi) AREG depletion also resulted in the appearance of anaphase bridges not detected in controls. **C,** (i) Graph of AREG qPCR following transfections. (ii) qPCR for IFN-like pathway genes in *BRCA2*$^{mut/+}$ MECs and (iii) non-carrier MECs 72hrs following siNT and siAREG transfection. **p<.01 ***p<.001; ****p<.0001; One-way ANOVA. Bars are S.E.M. **D,** *BRCA2*$^{mut/+}$ MECs were transfected as shown and treated for 4 days with 15uM HU followed by detection of SAβ-gal activity and imaging. Magnification of boxed regions are shown below. Arrows indicate SAβ-gal activity-positive MECs with typical senescent cell morphology. **E,** Quantification of SAβ-gal

positive MECs. Each data point represent the average of 50 SAβ-gal-positive MECs (n=250 cells per group). Bars are S.E.M. * p<.05 One-way ANOVA.

Figure 8. Chronic RS promotes nuclear AREG and induces expression of FOXM1 and ERα: *in vivo* correlations. A, RNA from *BRCA2*$^{mut/+}$ MECs treated with vehicle or 15µM HU for 4 days was used for qPCR to detect FOXM1, MYBL2 and ESR1 mRNA. Bars are S.E.M of 3 independent experiments. ****p<.0001; two-tailed t-test. **B,** Immunoblot of FOXM1, ERα, and AREG from control and MECs exposed to chronic RS. GAPDH detection was used as a protein loading control. **C,** AREG IHC in mammary gland tissue from MMTV-cre transgenic mice with *brca2*$^{+/+}$, *brca2*$^{+/f}$ or *brca2*$^{f/f}$ alleles shows detection of nuclear AREG in *brca2*$^{-/-}$ mammary ducts. Moderate to negative AREG staining was observed in *brca2*$^{+/+}$ and $^{-/-}$ glands. **D,** Examples of AREG IHC in patient mammary glands from non-carriers (i-iii) and *BRCA2*$^{mut/+}$ mammary glands (iv-ix). A range of nuclear AREG was present in histologically normal tissue from both patient groups (i-iv). Nuclear AREG was detected in the majority of *BRCA2*$^{mut/+}$ MECs in regions of mild dysplasia and hyperplastic ducts (v-vii). Higher magnification in viii and ix show nuclear AREG-positive cells in the luminal layer. **E,** ERα IHC in histologically normal mammary tissue from non-carriers and *BRCA2*$^{mut/+}$ glands (i-v) shows increased ERα-positive cells present in *BRCA2*$^{mut/+}$ lobules and ducts. Cells in hyperplastic lesions are largely ERα-positive. **F,** IHC shows predominantly nuclear FOXM1 present in a scattered MECs in histologically normal tissue from non-carriers (i, ii) and *BRCA2*$^{mut/+}$ glands (v). Small regions of dysplasia/hyperplasia in both patient groups contained increased levels of nuclear and cytoplasmic FOXM1 staining (iv, vi, vii). In contrast, cells in large hyperplastic lesions typically expressed little or no nuclear FOXM irrespective of *BRCA2* status (iii and vii).

1 Singh SS, Chauhan SB, Kumar A, Kumar S, Engwerda CR, Sundar S *et al.* Amphiregulin in cellular physiology, health, and disease: Potential use as a biomarker and therapeutic target. *Journal Cellular Physiology* 2022; **237**: 1143–1156.

2 Ciarloni L, Mallepell S, Brisken C. Amphiregulin is an essential mediator of estrogen receptor alpha function in mammary gland development. *Proc Natl Acad Sci U S A* 2007; **104**: 5455–5460.

3 Berasain C, Avila MA. Amphiregulin. *Semin Cell Dev Biol* 2014; **28**: 31–41.

4 Fukuda S, Nishida-Fukuda H, Nakayama H, Inoue H, Higashiyama S. Monoubiquitination of pro-amphiregulin regulates its endocytosis and ectodomain shedding. *Biochem Biophys Res Commun* 2012; **420**: 315–320.

5 Johnson GR, Saeki T, Auersperg N, Gordon AW, Shoyab M, Salomon DS *et al.* Response to and expression of amphiregulin by ovarian carcinoma and normal ovarian surface epithelial cells: nuclear localization of endogenous amphiregulin. *Biochem Biophys Res Commun* 1991; **180**: 481–488.

6 Kimura H. Schwannoma-derived growth factor must be transported into the nucleus to exert its mitogenic activity. *Proc Natl Acad Sci U S A* 1993; **90**: 2165–2169.

7 Olsnes S, Klingenberg O, Wie˛dłocha A. Transport of Exogenous Growth Factors and Cytokines to the Cytosol and to the Nucleus. *Physiological Reviews* 2003; **83**: 163–182.

8 Isokane M, Hieda M, Hirakawa S, Shudou M, Nakashiro K, Hashimoto K *et al.* Plasma-membrane-anchored growth factor pro-amphiregulin binds A-type lamin and regulates global transcription. *J Cell Sci* 2008; **121**: 3608–3618.

9 Padeken J, Methot SP, Gasser SM. Establishment of H3K9-methylated heterochromatin and its functions in tissue differentiation and maintenance. *Nat Rev Mol Cell Biol* 2022; **23**: 623–640.

10 Wang T, Xu C, Liu Y, Fan K, Li Z, Sun X *et al.* Crystal structure of the human SUV39H1 chromodomain and its recognition of histone H3K9me2/3. *PLoS One* 2012; **7**: e52977.

11 Bannister AJ, Zegerman P, Partridge JF, Miska EA, Thomas JO, Allshire RC *et al.* Selective recognition of methylated lysine 9 on histone H3 by the HP1 chromo domain. *Nature* 2001; **410**: 120–124.

12 Lachner M, O'Carroll D, Rea S, Mechtler K, Jenuwein T. Methylation of histone H3 lysine 9 creates a binding site for HP1 proteins. *Nature* 2001; **410**: 116–120.

13 Lopez-Contreras AJ, Ruppen I, Nieto-Soler M, Murga M, Rodriguez-Acebes S, Remeseiro S *et al.* A proteomic characterization of factors enriched at nascent DNA molecules. *Cell Rep* 2013; **3**: 1105–1116.

14 Canzio D, Chang EY, Shankar S, Kuchenbecker KM, Simon MD, Madhani HD *et al.* Chromodomain-mediated oligomerization of HP1 suggests a nucleosome-bridging mechanism for heterochromatin assembly. *Mol Cell* 2011; **41**: 67–81.

15 Schotta G, Ebert A, Krauss V, Fischer A, Hoffmann J, Rea S *et al.* Central role of Drosophila SU(VAR)3-9 in histone H3-K9 methylation and heterochromatic gene silencing. *EMBO J* 2002; **21**: 1121–1131.

16 Janssen A, Colmenares SU, Karpen GH. Heterochromatin: Guardian of the Genome. *Annu Rev Cell Dev Biol* 2018; **34**: 265–288.

17 Grewal SIS. The molecular basis of heterochromatin assembly and epigenetic inheritance. *Mol Cell* 2023; **83**: 1767–1785.

18 de Koning APJ, Gu W, Castoe TA, Batzer MA, Pollock DD. Repetitive elements may comprise over two-thirds of the human genome. *PLoS Genet* 2011; **7**: e1002384.

19 Lander ES, Linton LM, Birren B, Nusbaum C, Zody MC, Baldwin J *et al.* Initial sequencing and analysis of the human genome. *Nature* 2001; **409**: 860–921.

20 Black JC, Allen A, Van Rechem C, Forbes E, Longworth M, Tschöp K *et al.* Conserved antagonism between JMJD2A/KDM4A and HP1γ during cell cycle progression. *Mol Cell* 2010; **40**: 736–748.

21 Allshire RC, Madhani HD. Ten principles of heterochromatin formation and function. *Nat Rev Mol Cell Biol* 2018; **19**: 229–244.

22 Takahashi S, Miura H, Shibata T, Nagao K, Okumura K, Ogata M *et al.* Genome-wide stability of the DNA replication program in single mammalian cells. *Nat Genet* 2019; **51**: 529–540.

23 Klein KN, Zhao PA, Lyu X, Sasaki T, Bartlett DA, Singh AM *et al.* Replication timing maintains the global epigenetic state in human cells. *Science* 2021; **372**: 371–378.

24 Guelen L, Pagie L, Brasset E, Meuleman W, Faza MB, Talhout W *et al.* Domain organization of human chromosomes revealed by mapping of nuclear lamina interactions. *Nature* 2008; **453**: 948–951.

25 Poleshko A, Mansfield KM, Burlingame CC, Andrake MD, Shah NR, Katz RA. The human protein PRR14 tethers heterochromatin to the nuclear lamina during interphase and mitotic exit. *Cell Rep* 2013; **5**: 292–301.

26 Solovei I, Wang AS, Thanisch K, Schmidt CS, Krebs S, Zwerger M *et al.* LBR and lamin A/C sequentially tether peripheral heterochromatin and inversely regulate differentiation. *Cell* 2013; **152**: 584–598.

27 Goldman RD, Shumaker DK, Erdos MR, Eriksson M, Goldman AE, Gordon LB *et al.* Accumulation of mutant lamin A causes progressive changes in nuclear architecture in Hutchinson–Gilford progeria syndrome. *Proc Natl Acad Sci USA* 2004; **101**: 8963–8968.

28 De Sandre-Giovannoli A, Bernard R, Cau P, Navarro C, Amiel J, Boccaccio I *et al.* Lamin A Truncation in Hutchinson-Gilford Progeria. *Science* 2003; **300**: 2055–2055.

29 Toth JI, Yang SH, Qiao X, Beigneux AP, Gelb MH, Moulson CL *et al.* Blocking protein farnesyltransferase improves nuclear shape in fibroblasts from humans with progeroid syndromes. *Proc Natl Acad Sci U S A* 2005; **102**: 12873–12878.

30 Liu B, Wang Z, Zhang L, Ghosh S, Zheng H, Zhou Z. Depleting the methyltransferase Suv39h1 improves DNA repair and extends lifespan in a progeria mouse model. *Nat Commun* 2013; **4**: 1868.

31 Gaillard H, García-Muse T, Aguilera A. Replication stress and cancer. *Nat Rev Cancer* 2015; **15**: 276–289.

32 Zeman MK, Cimprich KA. Causes and consequences of replication stress. *Nat Cell Biol* 2014; **16**: 2–9.

33 Schlacher K, Wu H, Jasin M. A distinct replication fork protection pathway connects Fanconi anemia tumor suppressors to RAD51-BRCA1/2. *Cancer Cell* 2012; **22**: 106–116.

34 Karaayvaz-Yildirim M, Silberman RE, Langenbucher A, Saladi SV, Ross KN, Zarcaro E *et al.* Aneuploidy and a deregulated DNA damage response suggest haploinsufficiency in breast tissues of BRCA2 mutation carriers. *Sci Adv* 2020; **6**: eaay2611.

35 Bhat KP, Cortez D. RPA and RAD51: fork reversal, fork protection, and genome stability. *Nat Struct Mol Biol* 2018; **25**: 446–453.

36 Feng W, Jasin M. BRCA2 suppresses replication stress-induced mitotic and G1 abnormalities through homologous recombination. *Nat Commun* 2017; **8**: 525.

37 Hashimoto Y, Ray Chaudhuri A, Lopes M, Costanzo V. Rad51 protects nascent DNA from Mre11-dependent degradation and promotes continuous DNA synthesis. *Nat Struct Mol Biol* 2010; **17**: 1305–1311.

38 Schlacher K, Christ N, Siaud N, Egashira A, Wu H, Jasin M. Double-strand break repair-independent role for BRCA2 in blocking stalled replication fork degradation by MRE11. *Cell* 2011; **145**: 529–542.

39 Feng G, Yuan Y, Li Z, Wang L, Zhang B, Luo J *et al.* Replication fork stalling elicits chromatin compaction for the stability of stalling replication forks. *Proc Natl Acad Sci U S A* 2019; **116**: 14563–14572.

40 Gaggioli V, Lo CSY, Reverón-Gómez N, Jasencakova Z, Domenech H, Nguyen H *et al.* Dynamic de novo heterochromatin assembly and disassembly at replication forks ensures fork stability. *Nat Cell Biol* 2023; **25**: 1017–1032.

41 Sun Y, Jiang X, Price BD. Tip60: Connecting chromatin to DNA damage signaling. *Cell Cycle* 2010; **9**: 930–936.

42 Ayrapetov MK, Gursoy-Yuzugullu O, Xu C, Xu Y, Price BD. DNA double-strand breaks promote methylation of histone H3 on lysine 9 and transient formation of repressive chromatin. *Proc Natl Acad Sci USA* 2014; **111**: 9169–9174.

43 Panico L, D'Antonio A, Salvatore G, Mezza E, Tortora G, De Laurentiis M *et al.* Differential immunohistochemical detection of transforming growth factor alpha, amphiregulin and CRIPTO in human normal and malignant breast tissues. *Int J Cancer* 1996; **65**: 51–56.

44 Yokoyama M, Ebert M, Funatomi H, Friess H, Buchler M, Johnson G *et al.* AMPHIREGULIN IS A POTENT MITOGEN IN HUMAN PANCREATIC-CANCER CELLS - CORRELATION WITH PATIENT SURVIVAL. *Int J Oncol* 1995. doi:10.3892/ijo.6.3.625.

45 Roux PP, Blenis J. ERK and p38 MAPK-activated protein kinases: a family of protein kinases with diverse biological functions. *Microbiol Mol Biol Rev* 2004; **68**: 320–344.

46 Wang Y, Tzeng Y-DT, Chang G, Wang X, Chen S. Amphiregulin retains ERα expression in acquired aromatase inhibitor resistant breast cancer cells. *Endocr Relat Cancer* 2020; **27**: 671–683.

47 González-Granado JM, Navarro-Puche A, Molina-Sanchez P, Blanco-Berrocal M, Viana R, De Mora JF *et al.* Sorting Nexin 6 Enhances Lamin A Synthesis and Incorporation into the Nuclear Envelope. *PLoS ONE* 2014; **9**: e115571.

48 Cavalli V, Vilbois F, Corti M, Marcote MJ, Tamura K, Karin M *et al.* The stress-induced MAP kinase p38 regulates endocytic trafficking via the GDI:Rab5 complex. *Mol Cell* 2001; **7**: 421–432.

49 Macé G, Miaczynska M, Zerial M, Nebreda AR. Phosphorylation of EEA1 by p38 MAP kinase regulates μ opioid receptor endocytosis. *EMBO J* 2005; **24**: 3235–3246.

50 Saldivar JC, Cortez D, Cimprich KA. The essential kinase ATR: ensuring faithful duplication of a challenging genome. *Nat Rev Mol Cell Biol* 2017; **18**: 622–636.

51 Simoneau A, Zou L. An extending ATR–CHK1 circuitry: the replication stress response and beyond. *Current Opinion in Genetics & Development* 2021; **71**: 92–98.

52 Shechter D, Costanzo V, Gautier J. ATR and ATM regulate the timing of DNA replication origin firing. *Nat Cell Biol* 2004; **6**: 648–655.

53 Toledo LI, Altmeyer M, Rask M-B, Lukas C, Larsen DH, Povlsen LK *et al.* ATR Prohibits Replication Catastrophe by Preventing Global Exhaustion of RPA. *Cell* 2013; **155**: 1088–1103.

54 King D, Southgate HED, Roetschke S, Gravells P, Fields L, Watson JB *et al.* Increased Replication Stress Determines ATR Inhibitor Sensitivity in Neuroblastoma Cells. *Cancers (Basel)* 2021; **13**: 6215.

55 Moiseeva T, Hood B, Schamus S, O'Connor MJ, Conrads TP, Bakkenist CJ. ATR kinase inhibition induces unscheduled origin firing through a Cdc7-dependent association between GINS and And-1. *Nat Commun* 2017; **8**: 1392.

56 Van Steensel B, Belmont AS. Lamina-Associated Domains: Links with Chromosome Architecture, Heterochromatin, and Gene Repression. *Cell* 2017; **169**: 780–791.

57 Briand N, Collas P. Lamina-associated domains: peripheral matters and internal affairs. *Genome Biol* 2020; **21**: 85.

58 Harr JC, Luperchio TR, Wong X, Cohen E, Wheelan SJ, Reddy KL. Directed targeting of chromatin to the nuclear lamina is mediated by chromatin state and A-type lamins. *Journal of Cell Biology* 2015; **208**: 33–52.

59 Ahn J, Jo I, Kang S, Hong S, Kim S, Jeong S *et al.* Structural basis for lamin assembly at the molecular level. *Nat Commun* 2019; **10**: 3757.

60 Liu J, Yin X, Liu B, Zheng H, Zhou G, Gong L *et al.* HP1α mediates defective heterochromatin repair and accelerates senescence in Zmpste24-deficient cells. *Cell Cycle* 2014; **13**: 1237–1247.

61 Raurell-Vila H, Bosch-Presegue L, Gonzalez J, Kane-Goldsmith N, Casal C, Brown JP *et al.* An HP1 isoform-specific feedback mechanism regulates Suv39h1 activity under stress conditions. *Epigenetics* 2017; **12**: 166–175.

62 Erdel F, Rademacher A, Vlijm R, Tünnermann J, Frank L, Weinmann R *et al.* Mouse Heterochromatin Adopts Digital Compaction States without Showing Hallmarks of HP1-Driven Liquid-Liquid Phase Separation. *Mol Cell* 2020; **78**: 236-249.e7.

63 Hamali B, Amine AAA, Al-Sady B. Regulation of the heterochromatin spreading reaction by *trans*- acting factors. *Open Biol* 2023; **13**: 230271.

64 Karaayvaz-Yildirim M, Silberman RE, Langenbucher A, Saladi SV, Ross KN, Zarcaro E *et al.* Aneuploidy and a deregulated DNA damage response suggest haploinsufficiency in breast tissues of BRCA2 mutation carriers. *Sci Adv* 2020; **6**: eaay2611.

65 Gaggioli V, Lo CSY, Reverón-Gómez N, Jasencakova Z, Domenech H, Nguyen H *et al.* Dynamic de novo heterochromatin assembly and disassembly at replication forks ensures fork stability. *Nat Cell Biol* 2023; **25**: 1017–1032.

66 Blow JJ, Ge X. Replication forks, chromatin loops and dormant replication origins. *Genome Biol* 2008; **9**: 244.

67 Dworak N, Makosa D, Chatterjee M, Jividen K, Yang C-S, Snow C *et al.* A nuclear lamina-chromatin-Ran GTPase axis modulates nuclear import and DNA damage signaling. *Aging Cell* 2019; **18**: e12851.

68 Moudry P, Lukas C, Macurek L, Neumann B, Heriche J-K, Pepperkok R *et al.* Nucleoporin NUP153 guards genome integrity by promoting nuclear import of 53BP1. *Cell Death Differ* 2012; **19**: 798–807.

69 Galanty Y, Belotserkovskaya R, Coates J, Polo S, Miller KM, Jackson SP. Mammalian SUMO E3-ligases PIAS1 and PIAS4 promote responses to DNA double-strand breaks. *Nature* 2009; **462**: 935–939.

70 Spain BH, Larson CJ, Shihabuddin LS, Gage FH, Verma IM. Truncated BRCA2 is cytoplasmic: Implications for cancer-linked mutations. *Proc Natl Acad Sci USA* 1999; **96**: 13920–13925.

71 Yano K, Morotomi K, Saito H, Kato M, Matsuo F, Miki Y. Nuclear Localization Signals of the BRCA2 Protein. *Biochemical and Biophysical Research Communications* 2000; **270**: 171–175.

72 Shevelyov YY. Interactions of Chromatin with the Nuclear Lamina and Nuclear Pore Complexes. *Int J Mol Sci* 2023; **24**: 15771.

73 Stiekema M, Houben F, Verheyen F, Borgers M, Menzel J, Meschkat M *et al.* The Role of Lamins in the Nucleoplasmic Reticulum, a Pleiomorphic Organelle That Enhances Nucleo-Cytoplasmic Interplay. *Front Cell Dev Biol* 2022; **10**: 914286.

74 Vincent J, Adura C, Gao P, Luz A, Lama L, Asano Y *et al.* Small molecule inhibition of cGAS reduces interferon expression in primary macrophages from autoimmune mice. *Nat Commun* 2017; **8**: 750.

75 Mackenzie KJ, Carroll P, Martin C-A, Murina O, Fluteau A, Simpson DJ *et al.* cGAS surveillance of micronuclei links genome instability to innate immunity. *Nature* 2017; **548**: 461–465.

76 Yang H, Wang H, Ren J, Chen Q, Chen ZJ. cGAS is essential for cellular senescence. *Proc Natl Acad Sci U S A* 2017; **114**: E4612–E4620.

77 Montavon T, Shukeir N, Erikson G, Engist B, Onishi-Seebacher M, Ryan D *et al.* Complete loss of H3K9 methylation dissolves mouse heterochromatin organization. *Nat Commun* 2021; **12**: 4359.

78 Hansen AM, Ge Y, Schuster MB, Pundhir S, Jakobsen JS, Kalvisa A *et al.* H3K9 dimethylation safeguards cancer cells against activation of the interferon pathway. *Sci Adv* 2022; **8**: eabf8627.

79 Stoll SW, Stuart PE, Swindell WR, Tsoi LC, Li B, Gandarillas A *et al.* The EGF receptor ligand amphiregulin controls cell division via FoxM1. *Oncogene* 2016; **35**: 2075–2086.

80 Madureira PA, Varshochi R, Constantinidou D, Francis RE, Coombes RC, Yao K-M *et al.* The Forkhead Box M1 Protein Regulates the Transcription of the Estrogen Receptor α in Breast Cancer Cells. *Journal of Biological Chemistry* 2006; **281**: 25167–25176.

81 Hoogerbrugge N, Bult P, de Widt-Levert LM, Beex LV, Kiemeney LA, Ligtenberg MJL *et al.* High prevalence of premalignant lesions in prophylactically removed breasts from women at hereditary risk for breast cancer. *J Clin Oncol* 2003; **21**: 41–45.

82 Kauff ND, Brogi E, Scheuer L, Pathak DR, Borgen PI, Hudis CA *et al.* Epithelial lesions in prophylactic mastectomy specimens from women with BRCA mutations. *Cancer* 2003; **97**: 1601–1608.

83 Joyce R, Pascual R, Heitink L, Capaldo BD, Vaillant F, Christie M *et al.* Identification of aberrant luminal progenitors and mTORC1 as a potential breast cancer prevention target in BRCA2 mutation carriers. *Nat Cell Biol* 2024; **26**: 138–152.

84 Macheret M, Halazonetis TD. DNA replication stress as a hallmark of cancer. *Annu Rev Pathol* 2015; **10**: 425–448.

85 Yoshida R. Hereditary breast and ovarian cancer (HBOC): review of its molecular characteristics, screening, treatment, and prognosis. *Breast Cancer* 2021; **28**: 1167–1180.

86 Kuchenbaecker KB, Hopper JL, Barnes DR, Phillips K-A, Mooij TM, Roos-Blom M-J *et al.* Risks of Breast, Ovarian, and Contralateral Breast Cancer for *BRCA1* and *BRCA2* Mutation Carriers. *JAMA* 2017; **317**: 2402.

87 Pourmasoumi P, Moradi A, Bayat M. BRCA1/2 Mutations and Breast/Ovarian Cancer Risk: A New Insights Review. *Reprod Sci* 2024. doi:10.1007/s43032-024-01666-w.

88 Baldeyron C, Soria G, Roche D, Cook AJL, Almouzni G. HP1alpha recruitment to DNA damage by p150CAF-1 promotes homologous recombination repair. *J Cell Biol* 2011; **193**: 81–95.

89 Tomas A, Jones S, Vaughan SO, Hochhauser D, Futter CE. Stress-specific p38 MAPK activation is sufficient to drive EGFR endocytosis but not its nuclear translocation. *J Cell Sci* 2017; **130**: 2481–2490.

90 Chaumet A, Wright GD, Seet SH, Tham KM, Gounko NV, Bard F. Nuclear envelope-associated endosomes deliver surface proteins to the nucleus. *Nat Commun* 2015; **6**: 8218.

91 Barrowman J, Hamblet C, George CM, Michaelis S. Analysis of prelamin A biogenesis reveals the nucleus to be a CaaX processing compartment. *Mol Biol Cell* 2008; **19**: 5398–5408.

92 Bozler J, Nguyen HQ, Rogers GC, Bosco G. Condensins Exert Force on Chromatin-Nuclear Envelope Tethers to Mediate Nucleoplasmic Reticulum Formation in *Drosophila melanogaster*. *G3 Genes|Genomes|Genetics* 2015; **5**: 341–352.

93 Stephens AD, Liu PZ, Banigan EJ, Almassalha LM, Backman V, Adam SA *et al.* Chromatin histone modifications and rigidity affect nuclear morphology independent of lamins. *Mol Biol Cell* 2018; **29**: 220–233.

94 Snow CJ, Dar A, Dutta A, Kehlenbach RH, Paschal BM. Defective nuclear import of Tpr in Progeria reflects the Ran sensitivity of large cargo transport. *J Cell Biol* 2013; **201**: 541–557.

95 Drozdz MM, Vaux DJ. Shared mechanisms in physiological and pathological nucleoplasmic reticulum formation. *Nucleus* 2017; **8**: 34–45.

96 Xia Y, Ivanovska IL, Zhu K, Smith L, Irianto J, Pfeifer CR *et al.* Nuclear rupture at sites of high curvature compromises retention of DNA repair factors. *J Cell Biol* 2018; **217**: 3796–3808.

97 Kreienkamp R, Graziano S, Coll-Bonfill N, Bedia-Diaz G, Cybulla E, Vindigni A *et al.* A Cell-Intrinsic Interferon-like Response Links Replication Stress to Cellular Aging Caused by Progerin. *Cell Rep* 2018; **22**: 2006–2015.

98 Frisch SM, MacFawn IP. Type I interferons and related pathways in cell senescence. *Aging Cell* 2020; **19**: e13234.

99 Koromilas AE, Sexl V. The tumor suppressor function of STAT1 in breast cancer. *JAKSTAT* 2013; **2**: e23353.

100 Shalabi SF, Miyano M, Sayaman RW, Lopez JC, Jokela TA, Todhunter ME *et al.* Evidence for accelerated aging in mammary epithelia of women carrying germline BRCA1 or BRCA2 mutations. *Nat Aging* 2021; **1**: 838–849.

101 Joyce R, Pascual R, Heitink L, Capaldo BD, Vaillant F, Christie M *et al.* Identification of aberrant luminal progenitors and mTORC1 as a potential breast cancer prevention target in BRCA2 mutation carriers. *Nat Cell Biol* 2024; **26**: 138–152.

102 Stoll SW, Johnson JL, Li Y, Rittié L, Elder JT. Amphiregulin Carboxy-Terminal Domain Is Required for Autocrine Keratinocyte Growth. *Journal of Investigative Dermatology* 2010; **130**: 2031–2040.

103 Alvarez-Fernández M, Halim VA, Krenning L, Aprelia M, Mohammed S, Heck AJ *et al.* Recovery from a DNA-damage-induced G2 arrest requires Cdk-dependent activation of FoxM1. *EMBO Reports* 2010; **11**: 452–458.

104 Teh M-T, Gemenetzidis E, Chaplin T, Young BD, Philpott MP. Upregulation of FOXM1 induces genomic instability in human epidermal keratinocytes. *Mol Cancer* 2010; **9**: 45.

105 Millour J, Constantinidou D, Stavropoulou AV, Wilson MSC, Myatt SS, Kwok JM-M *et al.* FOXM1 is a transcriptional target of ERalpha and has a critical role in breast cancer endocrine sensitivity and resistance. *Oncogene* 2010; **29**: 2983–2995.

106 Carr JR, Kiefer MM, Park HJ, Li J, Wang Z, Fontanarosa J *et al.* FoxM1 regulates mammary luminal cell fate. *Cell Rep* 2012; **1**: 715–729.

107 Lewis CM, Herbert B-S, Bu D, Halloway S, Beck A, Shadeo A *et al.* Telomerase immortalization of human mammary epithelial cells derived from a BRCA2 mutation carrier. *Breast Cancer Res Treat* 2006; **99**: 103–115.

108 Boutet-Robinet E, Trouche D, Canitrot Y. Neutral Comet Assay. *BIO-PROTOCOL* 2013; **3**. doi:10.21769/BioProtoc.915.

109 Walsh KD, Kato TA. Alkaline Comet Assay to Detect DNA Damage. In: Gotoh E (ed). *Chromosome Analysis*. Springer US: New York, NY, 2023, pp 65–72.

110 Espinosa-Jeffrey A, Blanchi B, Biancotti JC, Kumar S, Hirose M, Mandefro B *et al.* Efficient Generation of Viral and Integration-Free Human Induced Pluripotent Stem Cell-Derived Oligodendrocytes. *CP Stem Cell Biology* 2016; **38**. doi:10.1002/cpsc.11.

Figure 1 Jiang et al

A

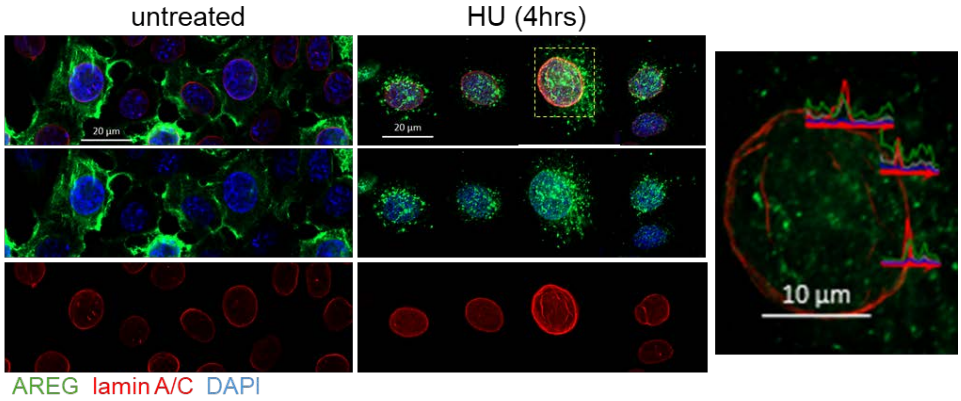

B

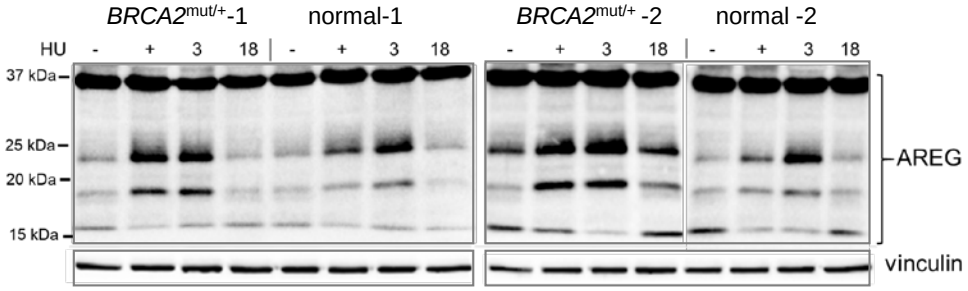

C

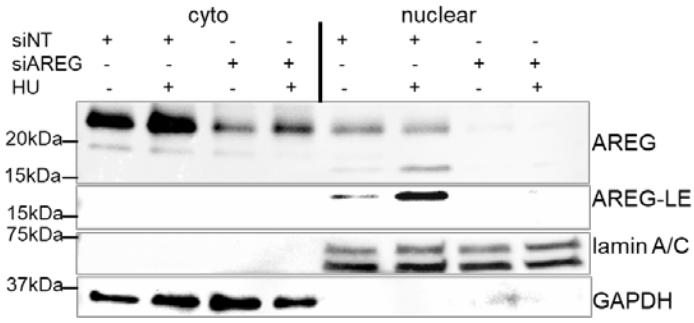

D

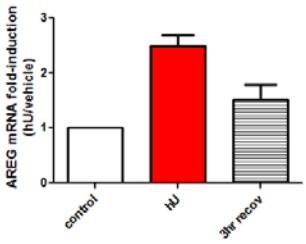

Figure 2 Jiang et al

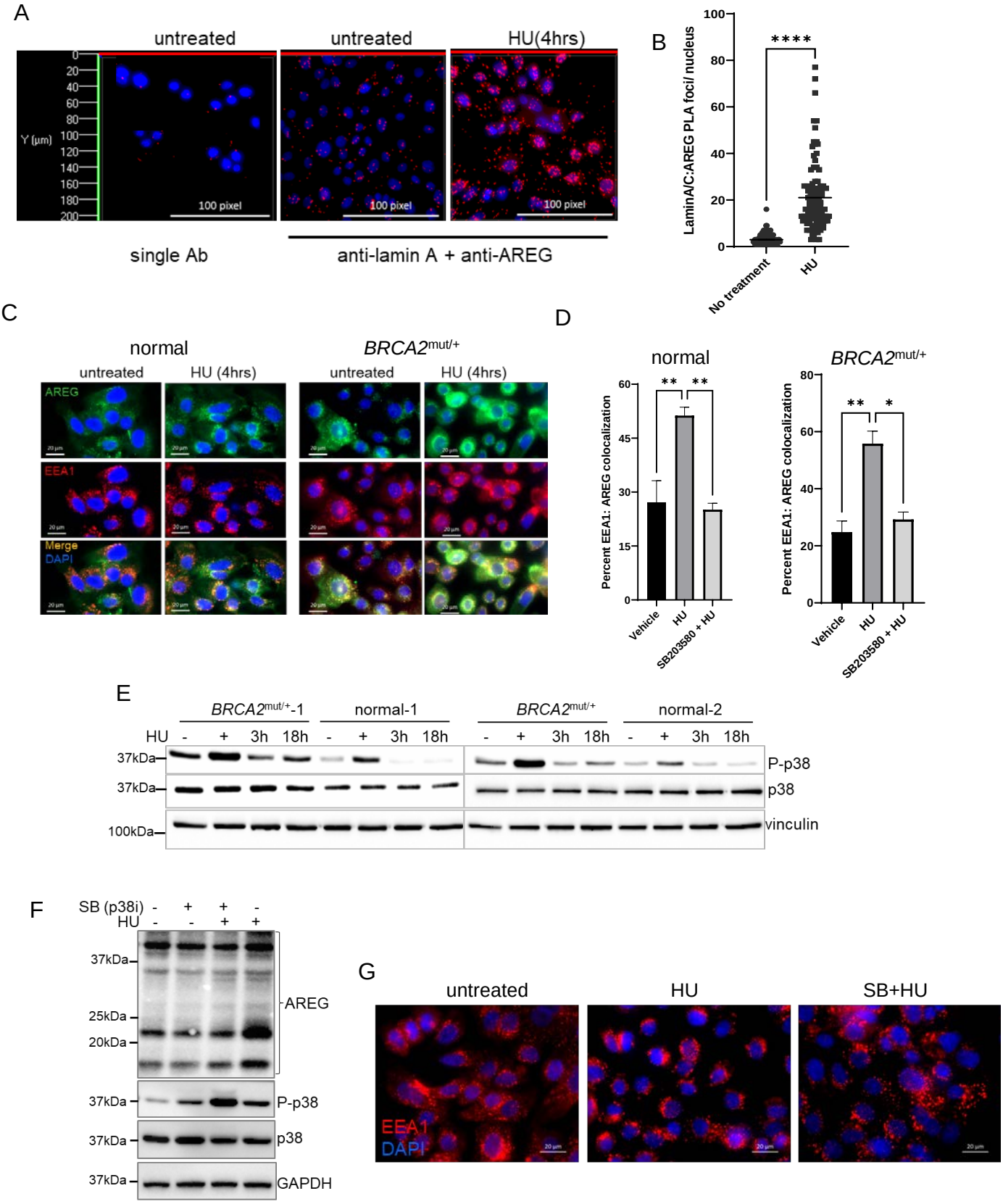

Figure 3 Jiang et al

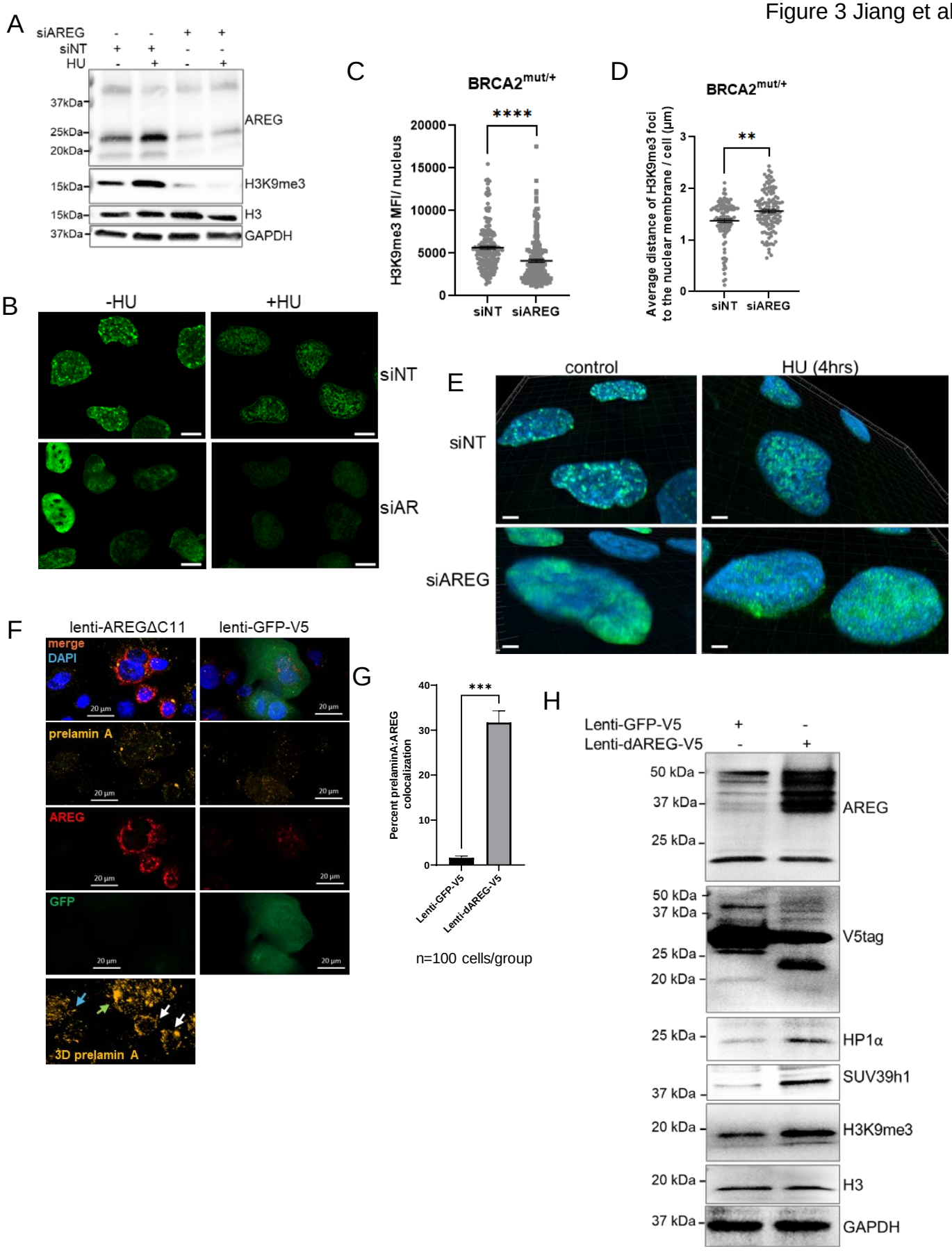

I

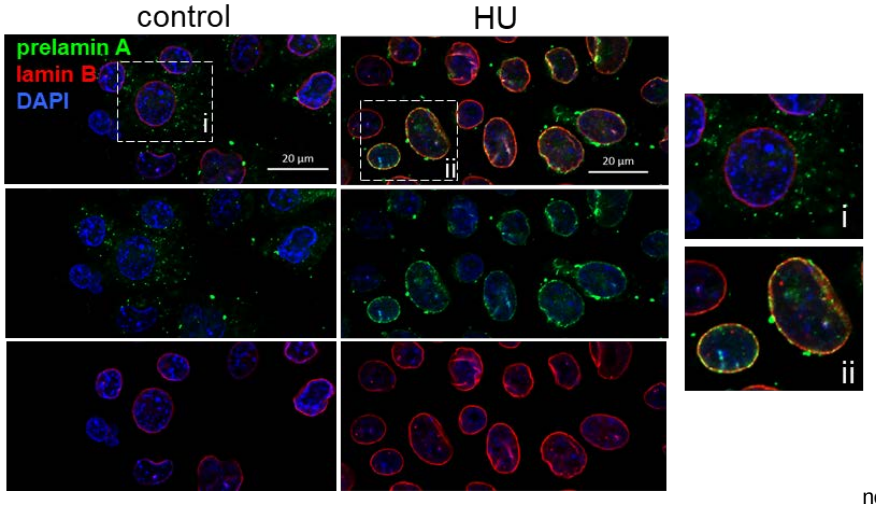

J

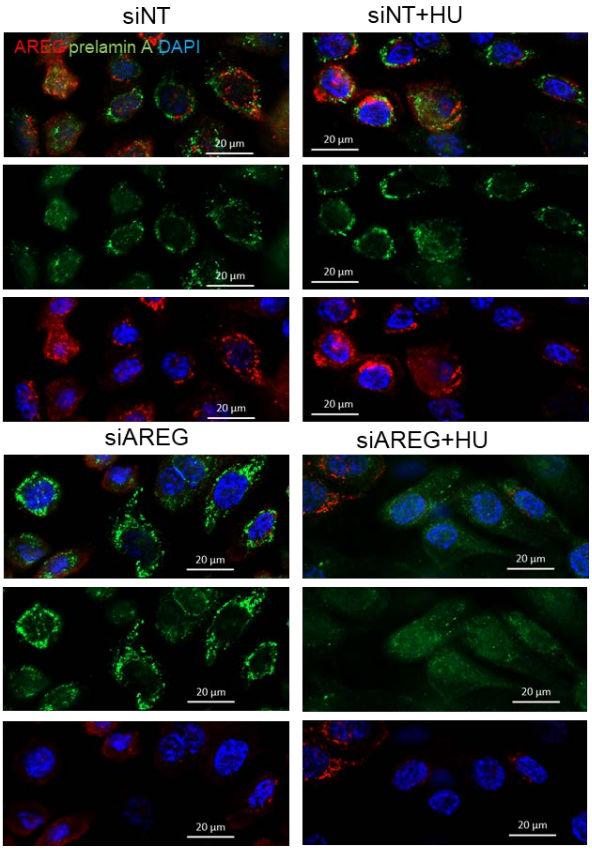

K

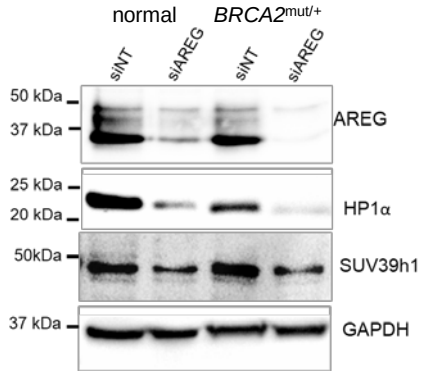

L

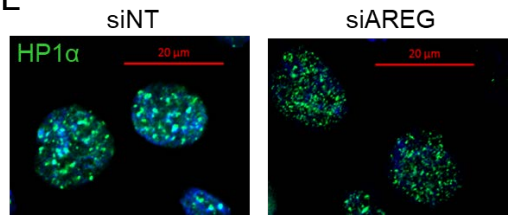

M

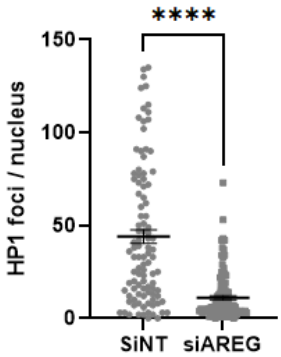

Foci threshold=0.5uM
n=100 cells/group

Figure 4 Jiang et al

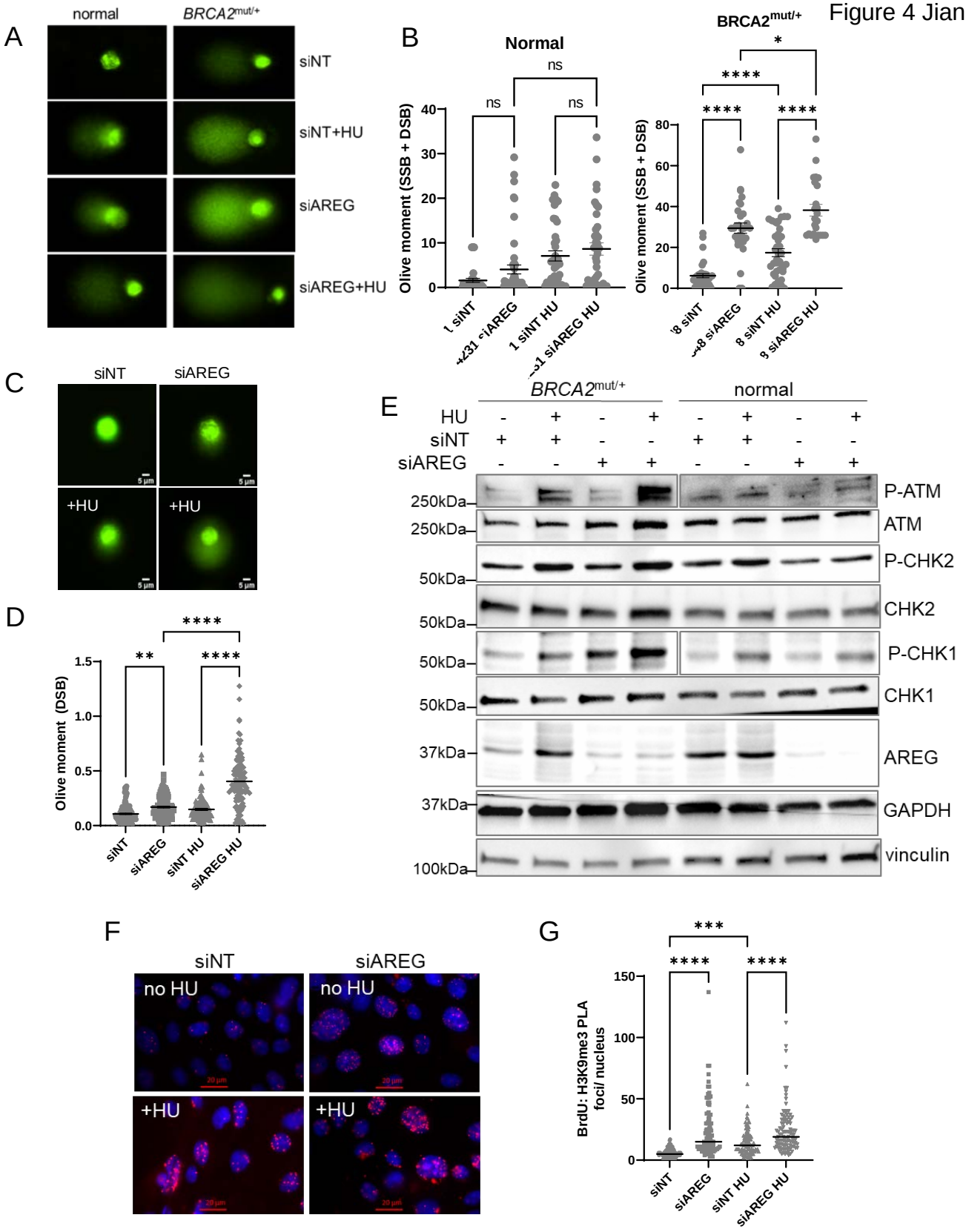

Figure 5 Jiang et al

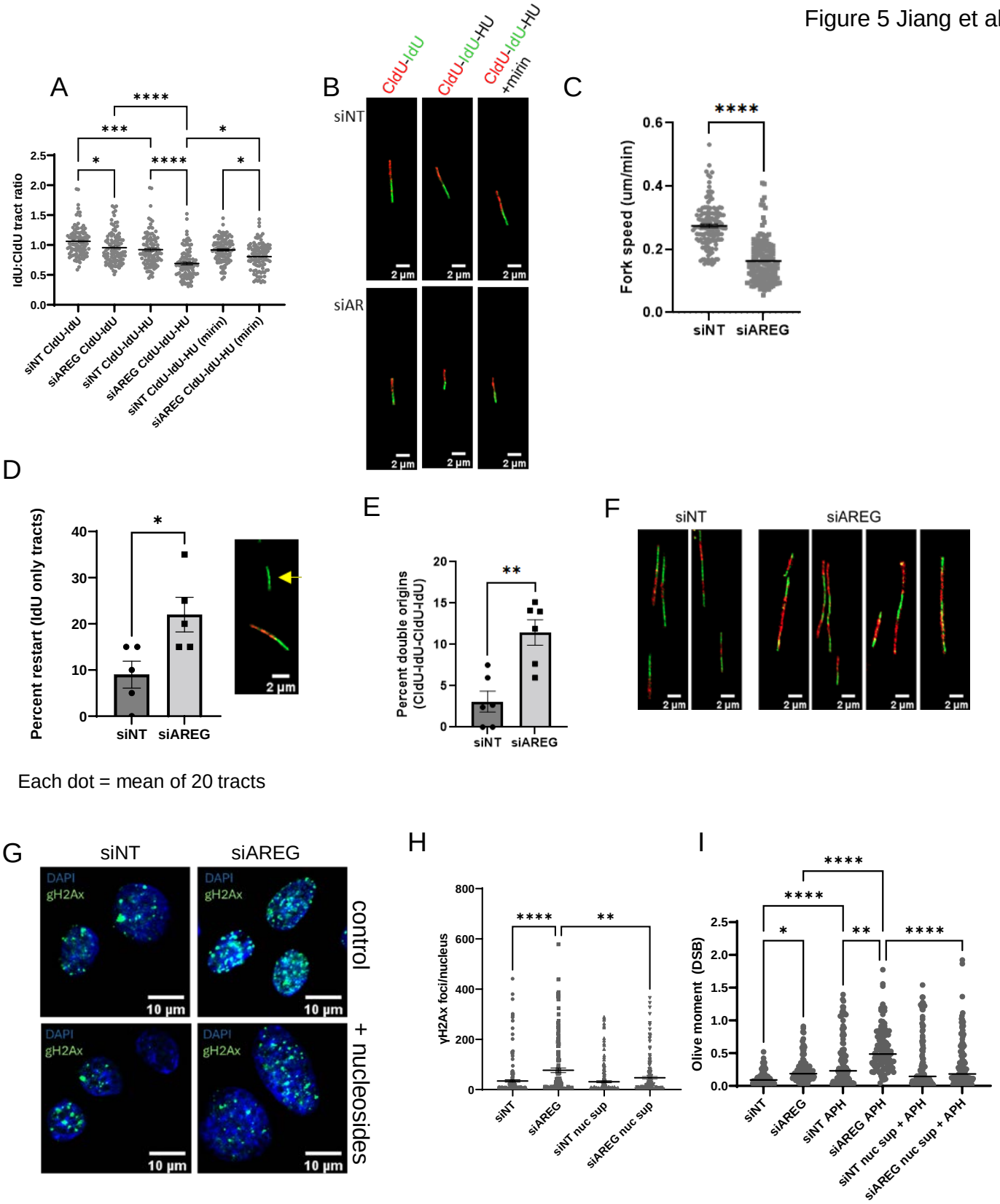

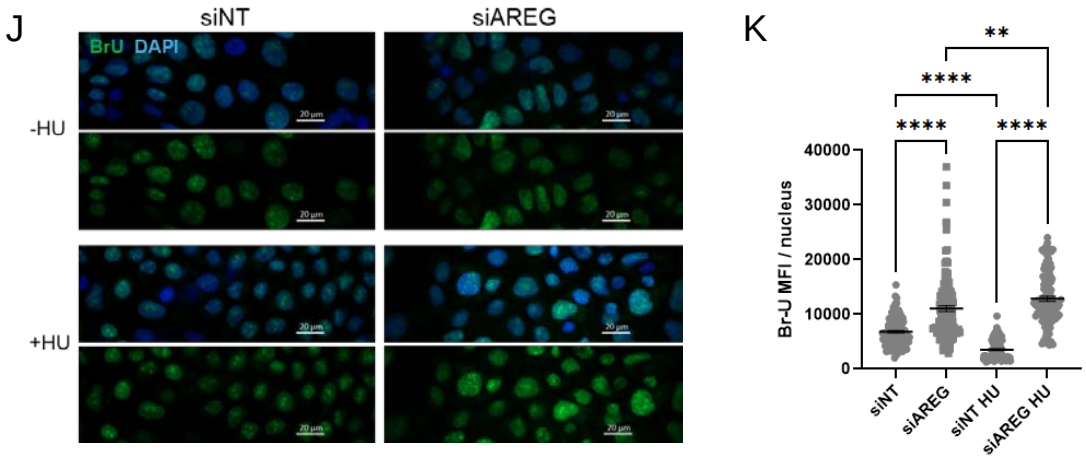
J
siNT
siAREG
BrU DAPI
-HU
+HU
20 µm
K
**
****
****
****
Br-U MFI / nucleus
40000
30000
20000
10000
0
siNT
siAREG
siNT HU
siAREG HU

Figure 6 Jiang et al

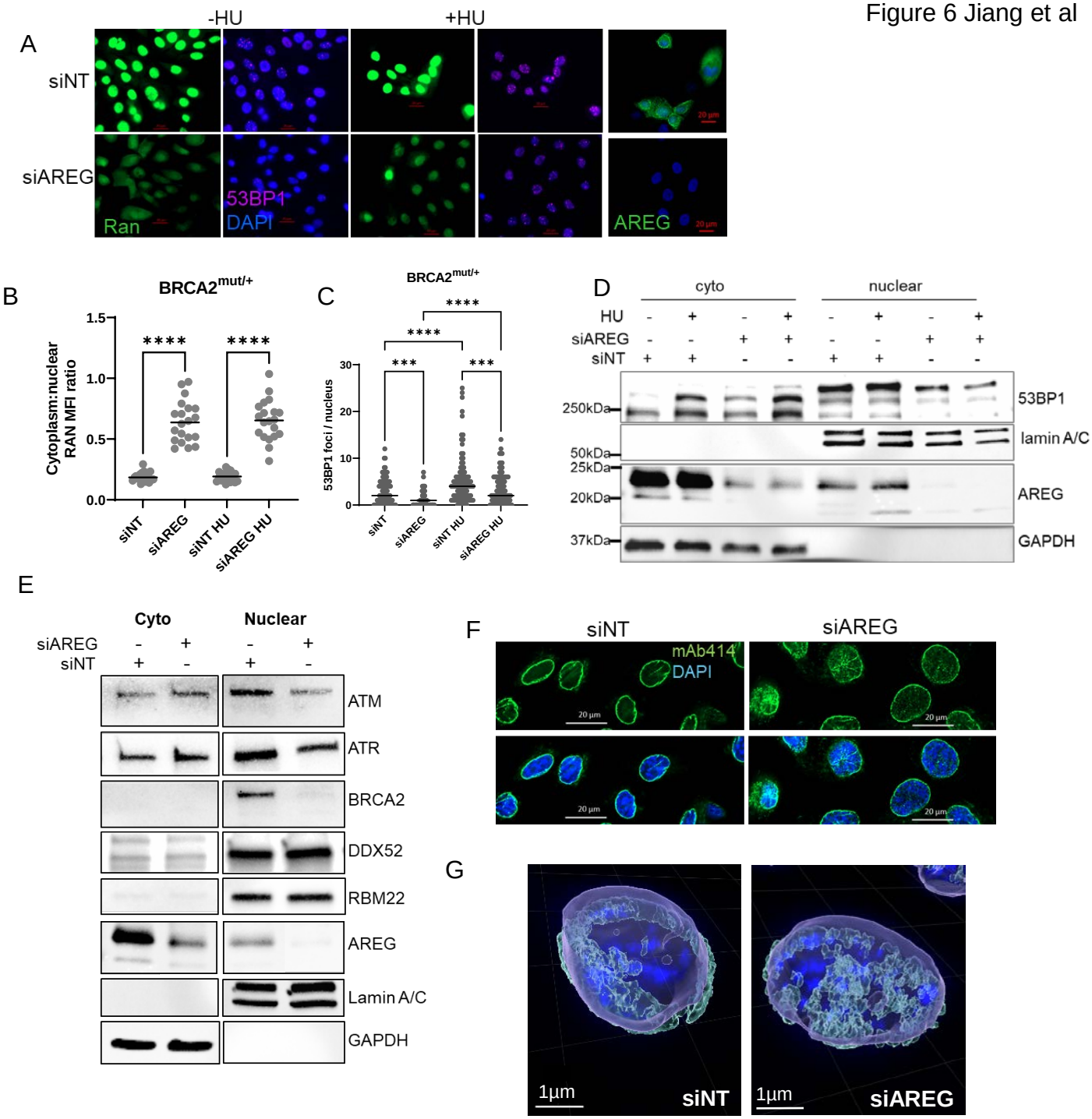

Figure 7 Jiang et al

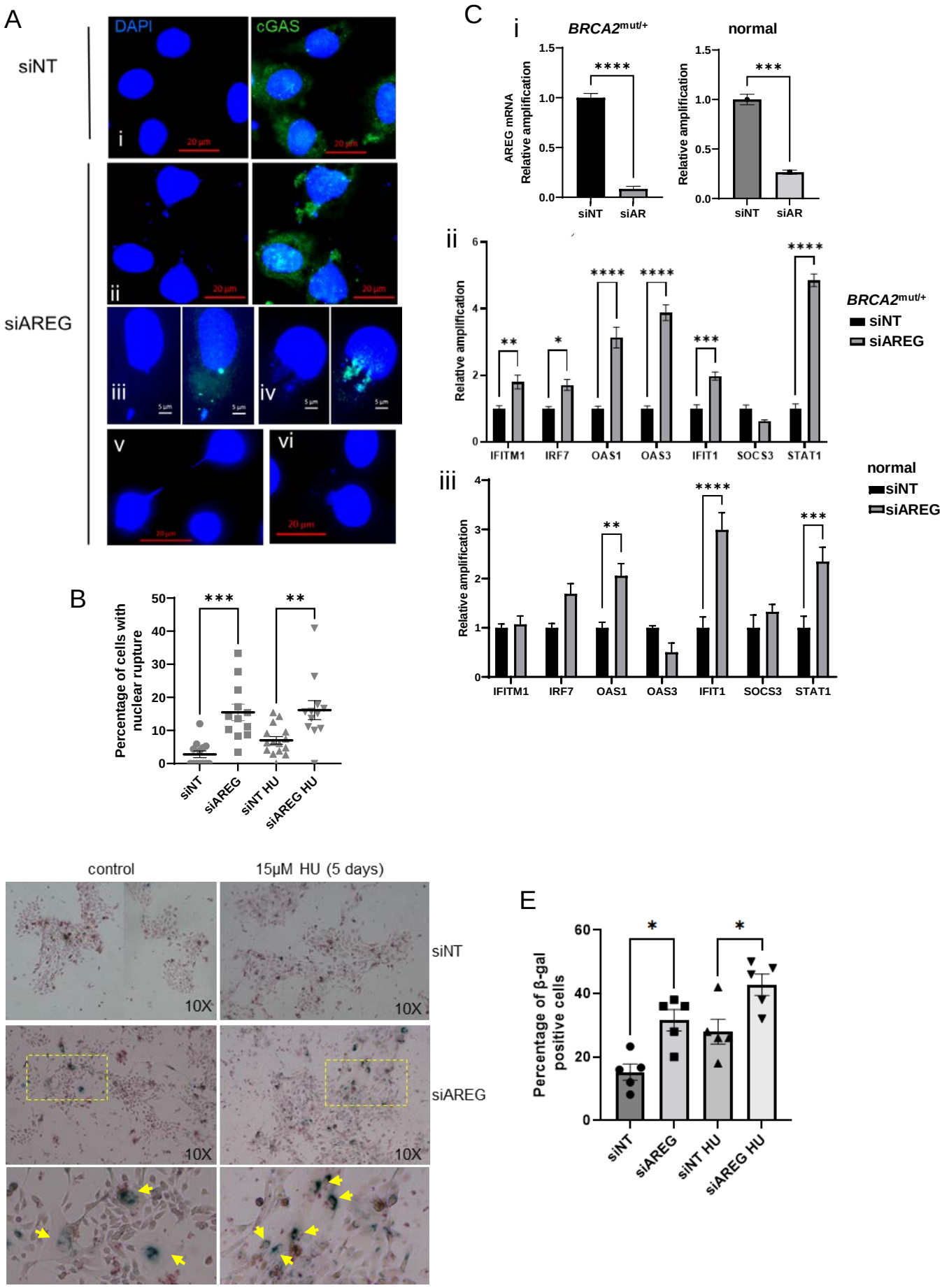

Figure 8 Jiang et al

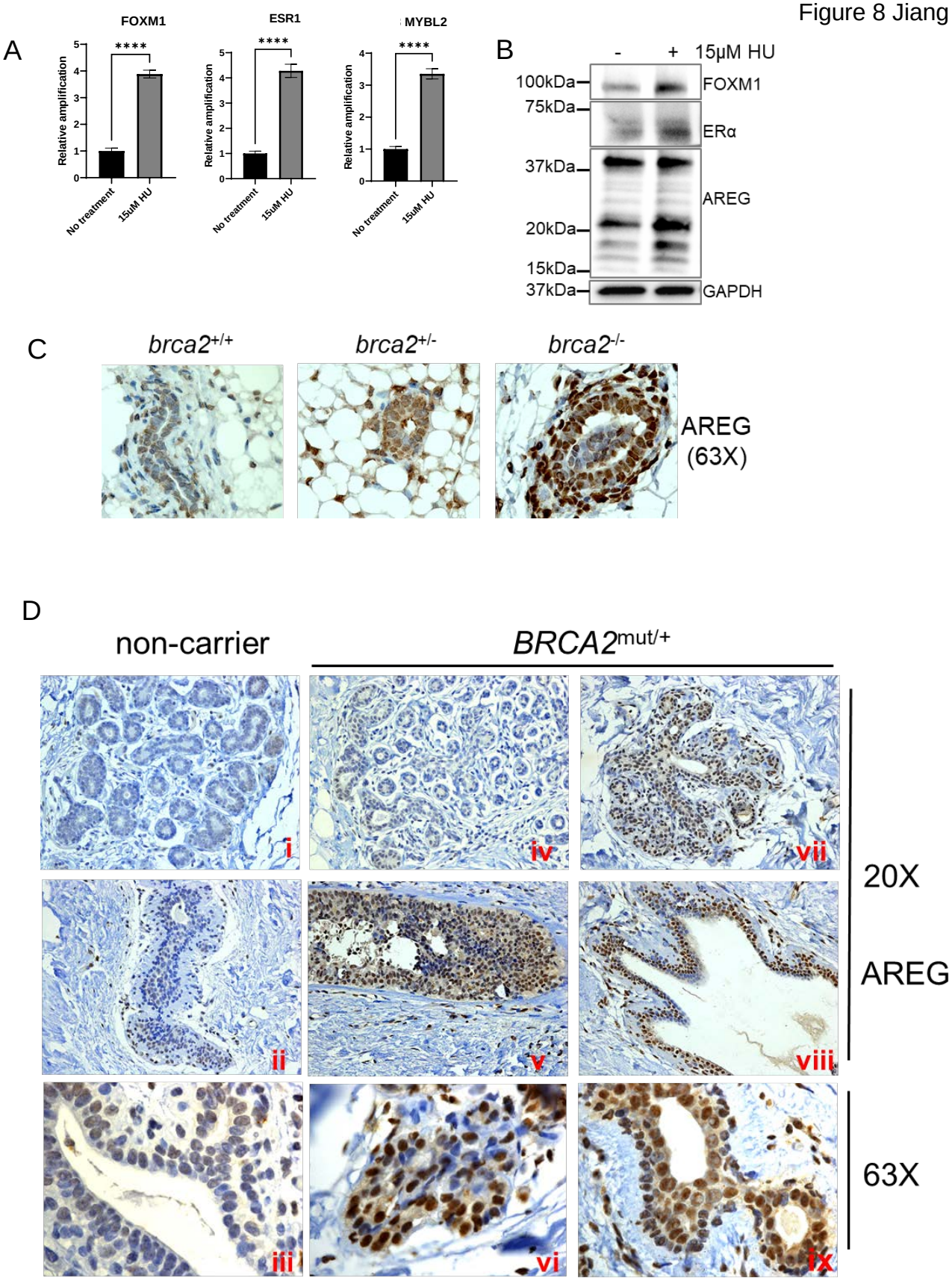

E

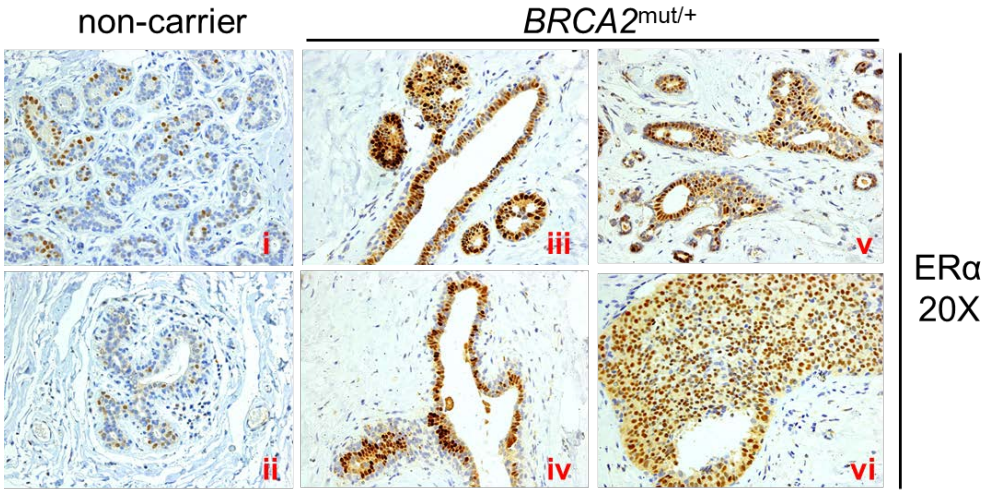
non-carrier
BRCA2mut/+
i
iii
v
ii
iv
vi
ERα
20X

F

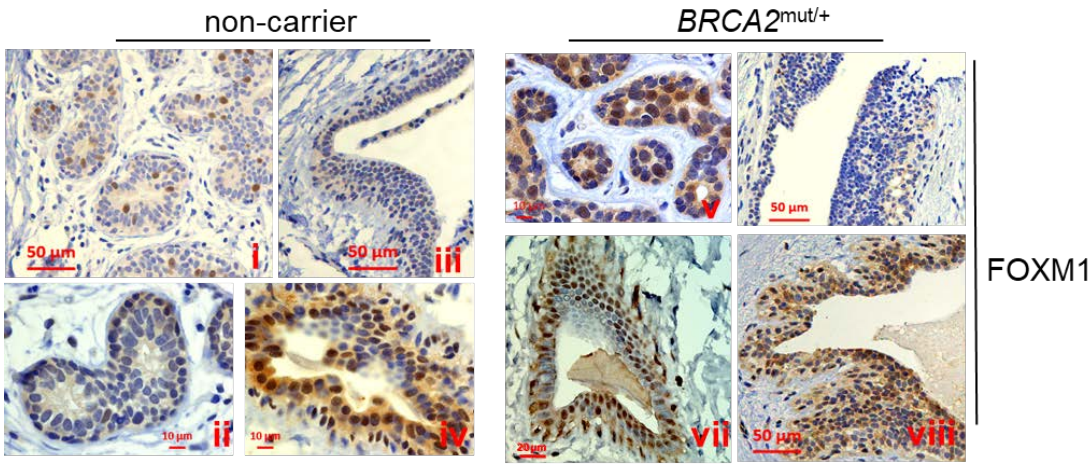
non-carrier
BRCA2mut/+
50 µm
i
50 µm
iii
v
50 µm
10 µm
ii
10 µm
iv
vii
20 µm
50 µm
viii
FOXM1